International Journal of Mechanical Sciences 307 (2025) 110769

Contents lists available at ScienceDirect

International Journal of Mechanical Sciences

journal homepage: www.elsevier.com/locate/ijmecsci

Anisotropic plastic deformation and damage evolution of sapphire under nanoindentation

Yuqiang Zhang [a,b,c], Zhongwei Hu [a,b,*], Yiqing Yu [b], Xipeng Xu [a,b,*], Xintian Cai [d,e], Qing Peng [f,*], Wenhan Zeng [c], Wenbin Zhong [c], Liam Blunt [c], Xiangqian Jiang [c]

[a] Institute of Manufacturing Engineering, Huaqiao University, Xiamen, 361021 China
[b] State Key Laboratory for High Performance Tools, Huaqiao University, Xiamen, China
[c] EPSRC Future Metrology Hub, Centre for Precision Technologies, School of Computing and Engineering, University of Huddersfield, UK
[d] School of Mechanical Engineering, Hubei University of Technology, Wuhan, China
[e] Hubei Key Laboratory of Electronic Manufacturing and Packaging Integration, Wuhan University, Wuhan, China
[f] School of Power and Mechanical Engineering, Wuhan University, Wuhan 430072, China

ARTICLE INFO

Keywords:
Nanoindentation
Plastic deformation
Subsurface damage mechanisms
Sapphire
Slip-twinning competition
Damage evolution model

ABSTRACT

Sapphire has extensive applications in advanced manufacturing fields, including electronics and semiconductors. However, its pronounced anisotropy poses significant challenges for ultra-precision machining and effective damage control. This study systematically investigates the anisotropic mechanisms of plastic deformation and subsurface damage (SSD) evolution across different sapphire crystal planes. This is achieved using molecular dynamics simulations, nanoindentation experiments, and transmission electron microscopy characterization. The results definitively show that distinct slip system behaviors depend on crystal orientation: the basal plane acts as the primary slip plane for the A/M/R-planes, whereas the rhombohedral slip is dominant for the C-plane. Subsurface damage of the A/M-planes is dominated by the formation of dislocation loops, whereas the C/R-planes primarily exhibit cross-slips. It was also identified that crack initiation and propagation mechanisms are closely linked to twinning behaviors. Cracks preferentially nucleate and propagate along the twinning planes, with basal and rhombohedral twinning playing key roles. The formation and evolution of SSD are significantly influenced by the activation and interaction of slip systems, leading to variations in damage depth, with a clear trend of M-plane > A-plane > R-plane. On the C-plane, basal slip initially minimizes damage; however, increased indentation depth activates rhombohedral slip, exacerbating SSD. Furthermore, a theoretical slip system activation model was successfully developed and validated, accurately predicting SSD evolution. These findings provide a robust theoretical basis for optimizing low-damage ultra-precision machining processes for sapphire and other anisotropic crystalline materials.

1. Introduction

Sapphire (α-Al_2O_3) is renowned for its exceptional mechanical strength, chemical inertness, and thermal stability, making it indispensable in high-performance applications such as microelectronics, optics, and thermal management for semiconductor substrates [1–4]. Sapphire is commonly utilized in four primary crystallographic orientations, namely the A, C, M and R-planes. Each orientation exhibits unique properties and applications. The A-plane is considered an ideal material for infrared windows due to its enhanced transmittance [5–7]. The C-plane is the most employed substrate in LED manufacturing [8–10]. Additionally, the M-plane demonstrates excellent potential in solar-blind ultraviolet detection [11–13], and the R-plane is the preferred substrate for silicon heteroepitaxy deposition [14–16]. Despite the clear attributes of sapphire as a functional material, significant anisotropy in its mechanical properties leads to different responses to plastic deformation and damage along different crystallographic directions, particularly at small-scale deformations. This anisotropy is crucial in determining how sapphire undergoes plastic deformation and how damage initiates and propagates under applied loads. Knowledge of these effects would give insights into the ultra-precision processing and applications of this material.

* Corresponding authors.
E-mail addresses: huzhongwei@hqu.edu.cn (Z. Hu), xpxu@hqu.edu.cn (X. Xu), pengqing@whu.edu.cn (Q. Peng).

https://doi.org/10.1016/j.ijmecsci.2025.110769
Received 29 June 2025; Received in revised form 28 August 2025; Accepted 28 August 2025
Available online 29 August 2025

Nanoindentation has emerged as a crucial technique for evaluating the mechanical properties of nanoscale materials [17–20], offering valuable insights into hardness [21,22], elastic modulus [23–25], and the behavior of plastic deformation [26–29]. For example, Li et al. [30] employed nanoindentation tests to determine the hardness, elastic modulus, fracture toughness, and maximum elastic recovery rate of YAG crystals. Yan et al. [31] conducted nanoindentation experiments on single-crystal silicon to investigate the damage, uncovering substantial amorphous and nanocrystalline in the subsurface region. Mitsuhiro et al. [32] studied nanoindentation-induced phase transitions in single-crystal 4H-SiC, demonstrating that the transition to 3C-SiC strongly depends on the orientation of the indenter relative to the crystal lattice. Furthermore, nanoindentation technology has also been applied to investigate the mechanical properties of various sapphire crystal planes, revealing the influence of crystal orientation on mechanical responses [33–36]. Researchers have explored the impact of indenter shape on the anisotropic nature of plastic deformation and crack propagation in sapphire [37–39]. As previously mentioned, the anisotropic crystal structure of sapphire significantly affects its plastic deformation under stress, but its subsurface damage (SSD) mechanisms remain insufficiently investigated. Although transmission electron microscopy (TEM) [40,41] has been widely used to reveal plastic deformation of materials, conducting dynamic deformation analysis at the atomic level remains a significant challenge.

Molecular dynamics (MD) simulations can overcome the inherent limitations of experimental and theoretical models [42–44], providing insights into plastic deformation and SSD evolution of sapphire at the atomic scale during processing [45–47]. Nishimura et al. [48] used MD simulations on three crystal orientations of aluminum oxide and found that the anisotropy of hardness could be attributed to dislocation activity linked to crystal orientation. Kim et al. [49] conducted nanoindentation simulations on four crystal planes (A/C/M/R) of sapphire, revealing that rhombohedral twinning occurred in the C-plane, while most slip systems were activated in the R-plane. Lin et al. [50] investigated the plastic deformation mechanism on the basal plane of sapphire under nanoindentation, analyzing surface morphology and dislocation nucleation conditions to understand crack formation on the sapphire surface. Xu et al. [51] explored nanoindentation behavior in four crystallographic orientations of sapphire using MD simulations. The detailed analysis of the dislocation mechanisms revealed that basal, rhombohedral, and pyramidal slips, as well as Rhombohedral twinning, are preferred during plastic deformation. Chen et al. [52] revisited the deformation behavior of the C-plane during nanoindentation and demonstrated that plasticity is achieved through alternating activation and annihilation of dislocation from active dislocation sources. Qiu et al. [53] studied how different Berkovich indenter orientations affect the hardness of the basal plane during nanoindentation. They found that when one edge of the indenter was perpendicular or parallel to the $[10\bar{1}0]$ orientation, the difference in hardness resulted from the variations in dislocation activation. Additionally, Eita et al. [54] reported dynamic twinning behavior dominated by atomic reorganization in α-Al_2O_3 using first-principles MD simulations. The results showed that twin propagation and annihilation were mediated by the migration of step structures on the matrix/twin interface. Despite the above studies having explored various mechanical behaviors of sapphire, a comprehensive understanding of the anisotropic deformation mechanisms in the subsurface remains unaddressed. For example, the damage evolution during plastic deformation, including the formation of slip bands, twins, and cracks [55–57], depends on crystal orientation and the nature of applied stress. Moreover, existing activation models of slip systems are unable to accurately predict damage evolution during indentation. Therefore, a deeper understanding of the plastic deformation of the subsurface in different sapphire crystal planes at the nanoscale, as well as the competition between slip and twinning during deformation, is crucial for accurately predicting and controlling its behavior in practical applications such as ultra-precision machining.

This paper utilizes MD simulations to perform nanoindentation on the A/C/M/R-planes of sapphire, elaborating on the plastic deformation behavior and the SSD anisotropy of different crystal orientations. The reliability of the MD simulations results was validated through corresponding experimental nanoindentation tests. An activation model of the sapphire crystal slip system was further established to accurately understand the influence of crystal anisotropy on the evolution of SSD during nanoindentation. Besides sapphire crystals, the model can serve as a theoretical foundation for low-damage processing of other anisotropic crystal materials.

The structure of the paper is as follows: Section 2 describes the molecular dynamics simulation setup and nanoindentation experiments. Section 3 presents and discusses simulation and experimental results, including load-displacement behavior, surface morphology, subsurface slip, dislocation, and twinning mechanisms. Section 4 introduces and validates a theoretical model for slip system activation and subsurface damage evolution. Finally, Section 5 summarizes the main conclusions and highlights the implications for low-damage machining of sapphire and other anisotropic crystals.

2. Methods

This section provides a detailed overview of the methodologies used in both the simulation and experimental studies of nanoindentation in sapphire. Section 2.1 describes the MD simulation model for nanoindentation, including the rationale behind the selection of key parameters such as system size, indentation velocity, and interatomic potential. Section 2.2 outlines the design of the corresponding nanoindentation experiments, detailing the specific procedures and testing conditions. By closely aligning the experimental setup with the simulation parameters, this study enables a comprehensive understanding of plastic deformation and damage evolution under indentation.

2.1. Simulation details

To observe the anisotropy of dynamic evolution of sapphire subsurface damage under nanoindentation experiment, the molecular dynamics simulations of nanoindentation were performed on different crystal planes of sapphire [58–60]. The unit lattice parameters of the hexagonal structure of sapphire are $a = b = 4.761$ Å, $c = 12.993$ Å, $\alpha = \beta = 90°$, and $\gamma = 120°$ [61–63], as shown in Fig. 1**(a)**. Fig. 1**(b)** presents a schematic diagram of the nanoindentation model. In the current simulation, the indenter was modeled as a hollow sphere and cylinder with a radius of 8 nm, while its loading speed was set 100 m/s (**Appendix A2** for detailed analysis) to minimize computational cost. To reduce the size effect of the sample [64,65], a sapphire cube with dimensions of approximately ($30 \times 30 \times 30$ nm) was constructed. The specific parameters were listed in Table 1. As in previous studies, all atoms were divided into three regions: boundary atoms, thermal atoms, and Newtonian atoms [66–68]. The thickness of the boundary and thermal layers was set to 1 nm. In addition, the distance between the indenter and the upper surface of the sapphire was set to 5 nm to reduce the influence of extraneous factors on the simulation results.

Selecting an appropriate potential function is crucial in the MD simulations. The Buckingham potential function has been successfully applied to characterize sapphire properties, such as phase transformation [69] and crystal growth [70], dislocation creep mechanisms [71], and surface characteristics [72]. The accuracy and applicability of the potential function used in this study have been verified. Detailed verification data are provided in **Appendix A1**. In addition, the interaction between the indenter and the workpiece was described by the Lennard-Jones [73] potential.

The simulations were conducted with periodic boundary conditions in the X and Y directions and fixed boundary conditions in the Z direction to replicate experimental conditions [74]. To ensure consistency

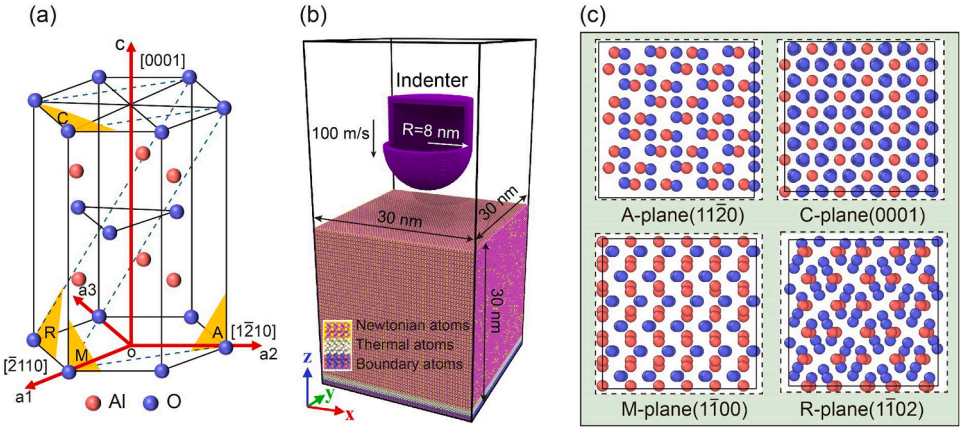

Fig. 1. The MD model of nanoindentation on sapphire. (a) Hexagonal crystal structure of sapphire (red balls represent Al atoms; blue balls represent O atoms); (b) Simulated model and sizes; (c) Atomic arrangement of the corresponding crystal planes (A-plane, C-plane, M-plane, R-plane) in Fig. 1(a).

Table 1
Simulated parameters employed in this study.

Parameters	Specimen: Sapphire				Indenter: Diamond
	A-plane	C-plane	M-plane	R-plane	
Dimensions (nm)	30 × 30 × 30				Radius: 8
Number of atoms	3216,780	3216,780	3129,840	3250,800	155,071
Time step (fs)	1				
Temperature (K)	297				
Depth (nm)	8				
Speed (m/s)	100 (+: loading, -: unloading)				

between simulations and experiments, both loading and unloading stages were included. All nanoindentation simulations were initially equilibrated through energy minimization, followed by relaxation at 297 K using an isothermal-isobaric ensemble. The temperature was maintained at 297 K during the nanoindentation using a Nosé-Hoover thermostat. The simulation results were visualized and analyzed with the Open Visualization Tool (OVITO) [75–77]. The dislocation extraction algorithm (DXA) analysis was used to reveal the slip and defects on subsurface of the material during the indentation process [78,79]. In single crystal sapphire, the oxygen (O) atoms form a hexagonal close-packed (HCP) structure, shown as red atomic regions in subsequent analysis. The white atoms and green regions represent the amorphous phase and face-centered cubic (FCC) structure of O atoms, respectively.

2.2. Experimental details

Nanoindentation tests are widely used to analyze deformation behavior of materials. To study the anisotropy of deformation behavior in sapphire, nanoindentation tests were conducted on the A-plane (11$\bar{2}$0), C-plane (0001), M-plane (1$\bar{1}$00), and R-plane (10$\bar{1}\bar{2}$) using a nano-indenter (Nano Indenter G200, USA), as shown in Fig. 2**(a)**. The experimental sample was a commercial polished wafer with dimensions of 10 × 10 × 0.43 mm as shown in Fig. 2**(b)**, that underwent chemical mechanical polishing resulting in a surface roughness Sa<0.7 nm, as shown in Fig. 2**(d)**. Hardness and elastic modulus, two critical parameters in nanoindentation tests, were measured in continuous stiffness mode using a Berkovich indenter with a 20 nm tip radius. The plastic deformation and crack growth modes of single crystal materials depend not only on the crystallographic properties of the sample but also on the shape of the indenter. Therefore, a spherical indenter with a 5 μm tip radius was utilized to study the deformation behavior of different crystal planes in quasi-static mode. The specific experimental conditions for the nanoindentation test are listed in Table 2. To minimize variability in the experimental results, each test was performed four times.

After the nanoindentation test, the surface morphology of the indentation was observed using a scanning electron microscope (SEM, HITACHI SU5000). For each crystal plane, two indentations were selected, and standard TEM samples (5 μm × 5 μm) were prepared along two crystallographic directions using a focused ion beam (FIB, Thermo Fisher Helios 5UX, USA), as shown in Fig. 2**(c)**. A TEM (FEI Talos F200X, USA) was then used to observe the microstructure of the sample, including lattice constants, crystal orientation, and crystal defects [80, 81].

3. Results and discussion

This section provides a comprehensive discussion of the MD simulation results, focusing on indentation force, surface morphology, and subsurface damage across different crystallographic orientations. The analysis includes slip formation, dislocation activity, and twinning-induced fracture, offering in-depth insight into the plastic deformation and damage evolution mechanisms of sapphire under nanoindentation. These findings are further supported by experimental characterizations using SEM and TEM.

3.1. Load-displacement curves

As the material enters the elastic–plastic deformation stage, key features such as pop-in events and corresponding load responses are analyzed to investigate the differences in deformation mechanisms across various crystallographic orientations of sapphire.

Fig. 3 shows the force-depth curves for four crystal planes: A/C/M/R-plane. All samples were deformed to a depth of $d = 8$ nm. All samples were deformed to a depth of $d = 8$ nm. The fluctuations in the curves are attributed to plastic rearrangement and strain hardening of the material [82]. At the same indentation depth, the A-plane exhibits the maximum load, with the corresponding order: A > M > C > R. Based on the load response, the curves can be described by the typical two deformation states. The first is the elastic stage, where the deformation curve is consistent with the Hertzian theoretical curve, as shown in the light orange area of Fig. 3. The subsequent plastic stage is characterized by dislocation nucleation, marked by the occurrence of pop-in events in the curves, as shown in the light blue area of Fig. 3. The pop-in phenomenon is clearly observed on the C-plane, while it is less evident on the other three crystal planes. In addition, the four crystal planes exhibit pop-in events at displacements of 1.07, 1.28, 0.94, and 1 nm, with corresponding loading forces of 2.14, 2.30, 1.76, and 2.14 nN, respectively.

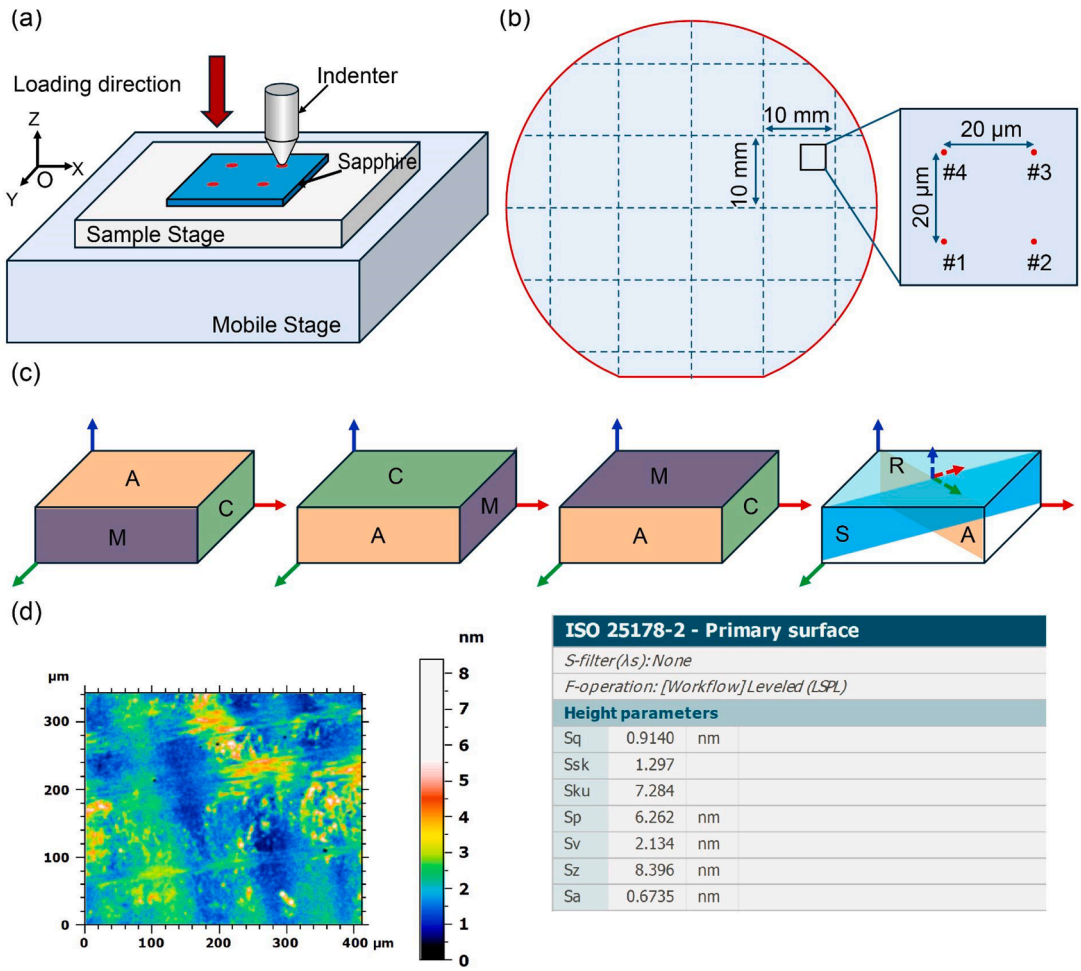

Fig. 2. Schematics of nanoindentation experiments. (a) Nanoindentation process; (b) Dimensions of sapphire wafer sample and the locations of the indentation; (c) The crystal directions corresponding to the four samples; (d) Measurement of surface roughness of the sapphire wafer using white light interferometry.

Table 2
Detailed experimental parameters for nanoindentation.

	Mode	Indenter radius	Crystal plane	Displacement	Strain rate
Hardness Young's modulus	continuous stiffness	20 nm	A/C/M/R-plane	500 nm	$0.05s^{-1}$
Deformation	quasi-static	5 μm			

The pop-in event of the C-plane occurs later than in the other three crystal planes, which is consistent with the experimental results (A: 154.8 nm; C: 188.89 nm; M: 131.32 nm; R: 153.78 nm). Detailed results are provided in Appendix A3. When the indenter was loaded to a certain depth, the curves exhibit a sharp drop followed by an upward trend, as highlighted by the black box in Fig. 3. This behavior is attributed to the activation of a slip system that propagates to the surface of the sample. The release of part of the stored energy during this process results in a temporary reduction in force, as indicated by the red dashed box in Fig. 3**(e)**.

3.2. Surface topography

The surface morphology serves as the most direct manifestation of its plastic deformation. By observing the surface morphology induced by nanoindentation, the symmetry and directional preference of shear strain patterns are analyzed to explore the intrinsic relationship between surface shear deformation and the anisotropic deformation mechanisms of sapphire.

Fig. 4**(a)** shows the shear strain distribution on the sapphire surface after unloading, visualized through color-coded atomic strain values. The indenter diameter is indicated by the white circle in the figure. Under spherical indentation, the shear strain on the four crystal planes exhibits anisotropic characteristics. Influenced by slip and twinning systems, shear strain on the A-plane predominantly occurs along the $[1\bar{1}00]$ direction. For the C-plane, the atomic strain displays a triple symmetry pattern with slip occurring along the $[\bar{1}010]$, $[1\bar{1}00]$, and $[01\bar{1}0]$ directions. On the M-plane and R-plane, shear strain tends to extend along the $[11\bar{2}0]$ direction. Therefore, the basal plane serves as the preferred slip plane for the A/M/R-planes, while the R-plane is the preferred slip plane for the C-plane.

Scanning electron microscopy (SEM) was used to assess the alterations in surface morphology induced by indentation, as shown in Fig. 4 **(b)**, where the crystal orientations correspond with MD simulations. Indentation on the A/M/R-plane produced linear streaks along the $[1\bar{1}00]/[11\bar{2}0]$ directions, which are attributed to basal twinning-induced surface features [83]. In contrast, no such streaks were observed on the C-plane because the basal twinning is parallel to the surface, making twinning traces undetectable. In addition, cracks were observed around the indentations, with crack propagation exhibiting anisotropic behavior. On the A-plane, the observed angles of crack formation are approximately 56.2° and 45° with the basal plane. Based on these interplanar angles, one set of cracks can be attributed to the R-plane, while the other set is likely determined by the direction of

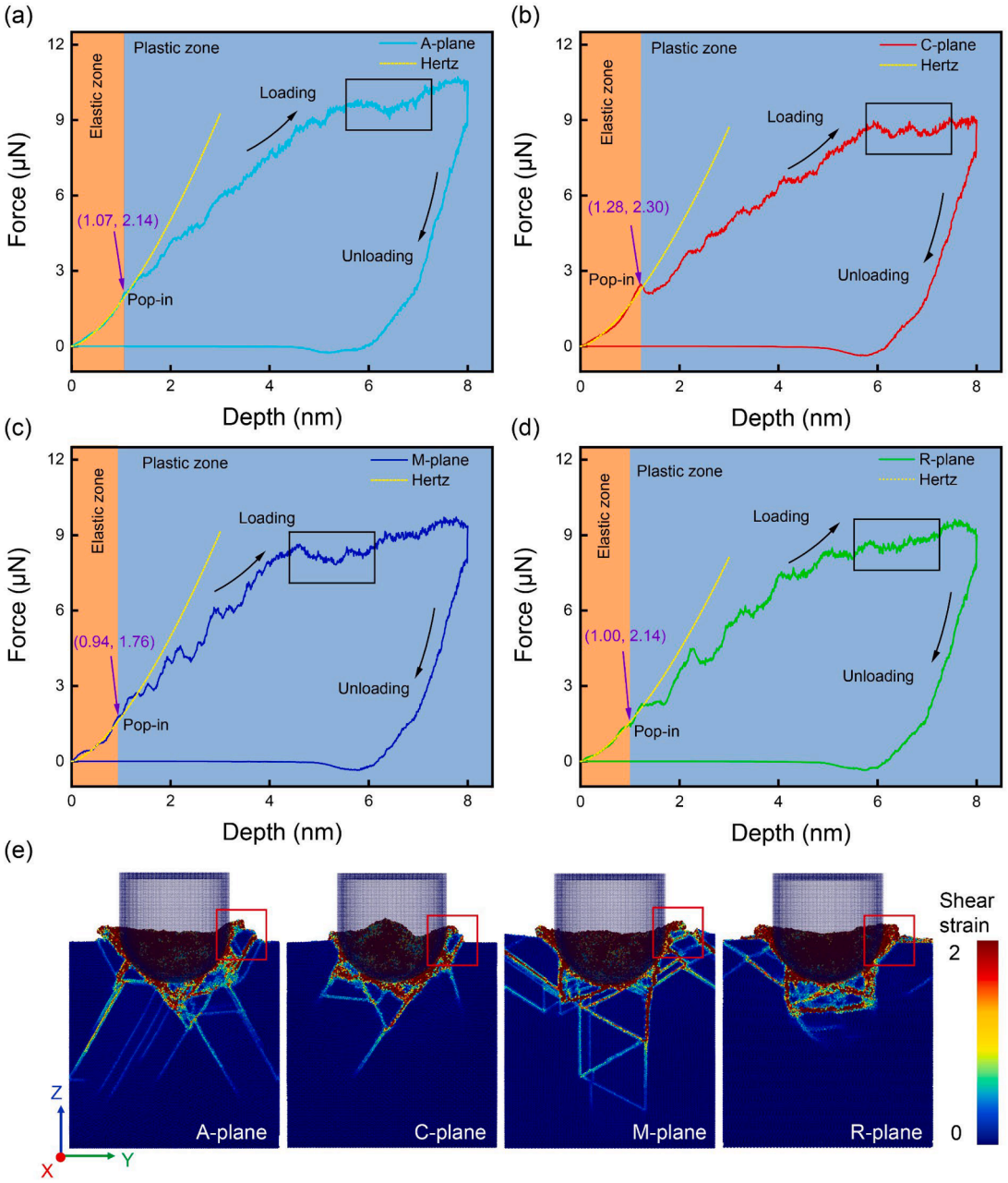

Fig. 3. Force-Displacement curves showing the loading and unloading process for four crystal plane MD nanoindentation tests. (a) A-plane; (b) C-plane; (c) M-plane; (d) R-plane; (e) The simulated shear strain diagram corresponding to the black box. Hertz fitting is added to show the elastic deformation process (yellow dashed line) a-d. The whole process is divided into two areas: Elastic zone (light orange); Plastic zone (light blue). Arrows clearly indicate pop-in events observed during loading.

maximum stress. Cracks on the C-plane form angles of 120° with each other, consistent with the projection of R-planes onto the C-plane, indicating that R-plane twinning nucleates the cracks and that prism slip governs their propagation direction [51]. On the M-plane, cracks form angles of approximately 53.8° with the C-plane and 36.2° with the A-plane. This suggests that the nucleation of cracks is governed by the R-plane. On the R-plane, cracks form a 45° angle with the reference edge. This indicates that basal twinning is the initiating factor for these cracks and that they propagate along the $[11\bar{2}0]$ direction.

The shear strain results from MD simulations are consistent with the twinning traces observed in the experiments. While the conditions for crack nucleation can be preliminarily predicted, a detailed fracture model requires further investigation.

3.3. *Damage mechanism of subsurface*

The plastic deformation in materials is mainly influenced by the movement of localized crystal slip systems and the formation of twinning [84,85]. By analyzing slip formation and twinning-induced cracking beneath the indentation, the subsurface damage mechanisms of sapphire across different crystallographic orientations are systematically investigated. For sapphire, the potential slip systems that can be activated during plastic deformation [36,86–88], as determined by its crystal structure, are listed in Table 3.

3.3.1. *Slip formation*

This section presents a detailed analysis of dislocation nucleation, motion, and interaction across different crystallographic orientations by examining slip system activation (CNA) and dislocation behavior (DXA).

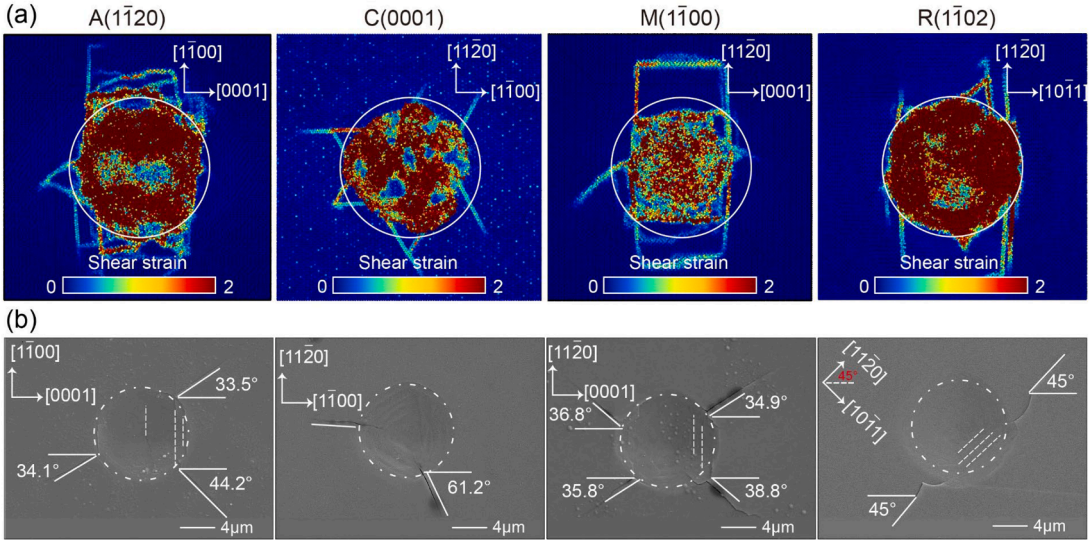

Fig. 4. The nanoindentation surface morphology of different crystal planes (A/C/M/R-plane): (a) Shear strain diagram of simulated morphology, the color intensity indicates the degree of shear deformation; (b) Experimental SEM image, the white dotted line indicates the indentation region created by the spherical indenter and the white dashed lines represent twinning streak.

Table 3
Slip systems are activated by plastic deformation of sapphire [36,86–88].

Types of slip systems	Slip planes	Slip directions	Plane spacing (d_{hkl})/ Å
Basal slip (BS)	{0001}	⟨1$\bar{1}$00⟩⟨11$\bar{2}$0⟩	12.991
Prismatic slip (PS)	{1$\bar{2}$10}	⟨1$\bar{1}$00⟩	2.380
	{10$\bar{1}$0}	⟨1$\bar{2}$10⟩	4.121
Rhombohedral slip (RS)	{10$\bar{1}$2}	⟨10$\bar{1}$1⟩⟨$\bar{2}$021⟩	3.483
	{11$\bar{2}$3}	⟨11$\bar{2}$0⟩⟨01$\bar{1}$0⟩	2.085
	{01$\bar{1}$1}	⟨10$\bar{1}$2⟩⟨1$\bar{2}$10⟩	3.928
	{01$\bar{1}$4}	⟨10$\bar{1}$1⟩	2.551

The CNA cross-sectional images of the A/C/M/R-planes along different crystal directions at various indentation depths are presented in Fig. 5. The cross-sectional view reveals that amorphized atoms are mainly distributed on both sides and below the indentation, extending into the matrix and the sample surface as the slip system moves. With the indentation depth increasing, the increased load leads to the activation of different slip systems in the subsurface regions of the A/C/M/R-planes. For example, a prismatic slip (PS) becomes apparent along the [0001] section of the A-plane. The angles between the slip direction and [1$\bar{1}$00] are 0°, 60°, and 120° However, the order of slip system activation differs. Along the [1$\bar{1}$00] section of the A-plane, the slip primarily occurs along the basal plane, with the slip direction perpendicular to [0001]. Additionally, rhombohedral slip (RS) is observed, with its slip direction forming a 28.8° relative to [0001]. By analyzing the interplanar angles, it is determined that the slip system is on the (11$\bar{2}$3) plane. The subsurface of the C-plane shows various slips of different crystal planes. The angles between the slip planes and the basal plane are 42.3°, 57.6°, 61.2°, and 90°, respectively. Based on these characteristic angles, they are determined to be the {1$\bar{1}$02}, (1$\bar{2}$16), ($\bar{1}$2$\bar{1}$3), and {11$\bar{2}$0} planes, respectively. Among these, the slip on the {1$\bar{1}$02} and ($\bar{1}$2$\bar{1}$3) planes are dominant and continues to expand into the matrix. For the M-plane, the slip systems of the {1$\bar{1}$02} and (0001) planes are activated successively. The {2$\bar{1}\bar{1}$3} plane is activated last, contrary to the results observed by Xu [51]. The {11$\bar{2}$0} plane slip system cross-slips on the (0001) plane, as shown in Fig. 6. Along the (11$\bar{2}$0) section, the {1$\bar{1}$02} slip system interacts with the BS systems, propagating continuously into the matrix. Similarly, {1$\bar{1}$02} rhombohedral slip is activated below the contact area of the R-plane, accompanied by slip along the (01$\bar{1}$0), (12$\bar{3}\bar{4}$), and (11$\bar{2}$0) planes. The interaction of these slip systems makes the SSD distribution on the R-plane highly complex.

Dislocation behavior during plastic deformation is a critical factor influencing subsurface damage, making dislocation analysis indispensable. The DXA cross-sectional images of the A/C/M/R-plane at various indentation depths, as shown in Fig. 6. After the transition from elastic to plastic deformation, the dislocation nucleation initially triggered by different crystal planes is different. For A-plane, initially only one dislocation line with a Burgers vector of $1/3\langle 1\bar{2}10\rangle$ appears below the indentation. The Miller index analysis confirms this as the $(1\bar{2}10)$ plane. In the case of the C-plane, indentation first induces a dislocation line with a Burgers vector of $1/3\langle 10\bar{1}0\rangle$, aligned parallel to the (0001) plane. The initial dislocation nucleation for the M-plane occurs at an indentation depth of 0.9 nm, with a dislocation Burgers vector of $1/3\langle 10\bar{1}0\rangle$, nucleating on the $(\bar{1}2\bar{1}0)$ plane, propagating along it. At an indentation depth of 1 nm, the R-plane initiates the nucleation of a $1/3\langle 1\bar{2}10\rangle$ dislocation, which slips along the (0001) plane.

As the indentation depth increases, nucleated dislocations radially expand along the most favorable slip planes, with a-type dislocations (green and orange) dominating conventional slip in sapphire. However, different crystal orientations produce distinct subsurface dislocation structures. Under A/M-plane loading, local a-type dislocation loops (Burger's vector $1/3\langle 1\bar{2}10\rangle$) form just beneath the surface and extend along $\langle 10\bar{1}0\rangle$ or $\langle 1\bar{2}10\rangle$. This occurs because sufficiently high local stresses cause dislocation sources near the surface to nucleate dislocation half-loops. Stress concentrations at the indentation surface, combined with the increasing number of nucleation sites, lead screw dislocations to dissociate into two partial dislocations on the basal plane ($1/3 < 1\bar{2}10 \geq 1/3\langle 10\bar{1}0\rangle + 1/3\langle 0\bar{1}10\rangle$) to reduce the Peierls barrier. As more dislocation loops nucleate, a "forest" of dislocations forms, impeding main slip and raising the yield stress (strain hardening). Under C-plane loading, basal slip traces appear first—due to the low generalized stacking fault energy (GSFE) of the basal plane (as shown in **Fig. A1**)—followed by rhombohedral slip at 57.6° As indentation depth increases, the screw components of a-type dislocations cross-slip onto rhombohedral planes, which also contain the $\langle 1\bar{2}10\rangle$ direction. The loading of C-plane rapidly builds strain along the c-axis, nucleating pure $\langle 0001\rangle$ screw dislocations. However, they encounter high GSFE on prism planes, making slip difficult. Under high stress, $\langle a + c\rangle$ dislocations ($1/3\langle 1\bar{2}10\rangle + 1/3 < 0001 \geq 1/3\langle 1\bar{2}13\rangle$) nucleate directly, relieving

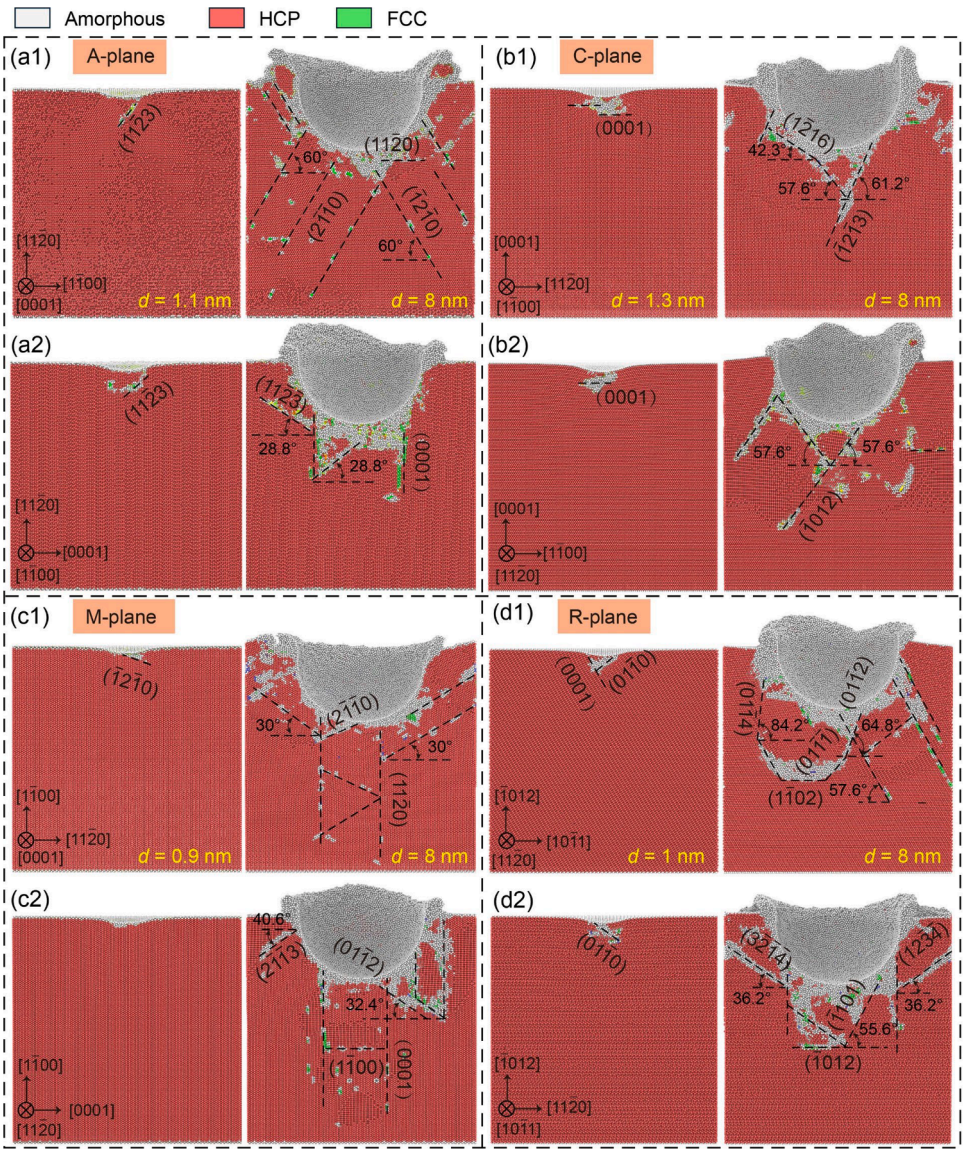

Fig. 5. Subsurface CNA analysis of sapphire after nanoindentation on different crystallographic planes across various cross-sections. (a-d) Crystalline phase transformations at different depths, including the critical depth for the elastic-plastic transition and at 8 nm (white represents amorphous phase, red represents HCP structure, and green represents FCC structure).

stress and promoting plastic deformation. These induced mixed dislocations typically nucleate at a specific depth beneath the contact zone and propagate along Rhombohedral planes, creating the characteristic subsurface dislocation network shown in Fig. 6**(b)**. The R-plane orientation, intermediate between the c- and a-axes, activates both basal and prism slip with comparable Schmid's factors. Consequently, sapphire can exhibit basal and prism dislocations simultaneously, interwoven in space. This configuration enables dislocations to switch between basal and prism planes. In R-plane samples, dislocation lines often kink within the crystal: a segment propagates on the basal plane, then turns onto a prism plane. This dual-plane slip creates a stepped dislocation structure, as shown in Fig. 6**(d)**. Analyzing these dislocation behaviors clarifies sapphire's plastic response on different crystal planes: limited plasticity arises from complex dislocation motions, yet the resulting strong interactions rapidly arrest further slip, underlying sapphire's intrinsic high strength and hardness.

To verify the origin and nature of subsurface damage identified in the MD simulations, TEM analysis was performed on samples after nanoindentation. Fig. 7 shows a TEM image of the subsurface region of the sapphire C-plane after indentation to a depth of 500 nm. The plastic damage zone contains defects such as stacking faults, lattice distortions, and deformation twinning. Numerous high-density stacking fault bands (marked by colored dashed lines) and a few cracks (circled in white) can be observed in Fig. 7**(a)**. These features indicate that the critical depth for the brittle-to-plastic transition of the C-plane has been exceeded at this indentation depth, validating the pop-in event observed in the load-displacement curve at approximately 200 nm. Fig. 7**(b)** presents the interplanar spacings of various crystallographic planes, corresponding well with the slip traces observed in Fig. 7**(a)**, and also confirms the slip systems identified in MDs. Fig. 7 **(c–e)** show high-resolution transmission electron microscopy (HR-TEM) images of selected plastic deformation regions. Specifically, Fig. 7**(d)** confirms the presence of R-plane twinning in the subsurface damage zone. Fig. 7 **(f–h)** display the Fast Fourier Transform (FFT) analyses of the areas highlighted by red squares in Fig. 7 **(c–e)**, further verifying the occurrence of basal slip (BS), rhombohedral slip (RS), and rhombohedral twinning (RT) beneath the indentation area on the C-plane. The TEM results along with an alternative crystallographic orientation are shown on Fig. 8, revealing similar analytical findings. For HR-TEM images and selected-area electron diffraction (SAED) analyses of the subsurface regions beneath

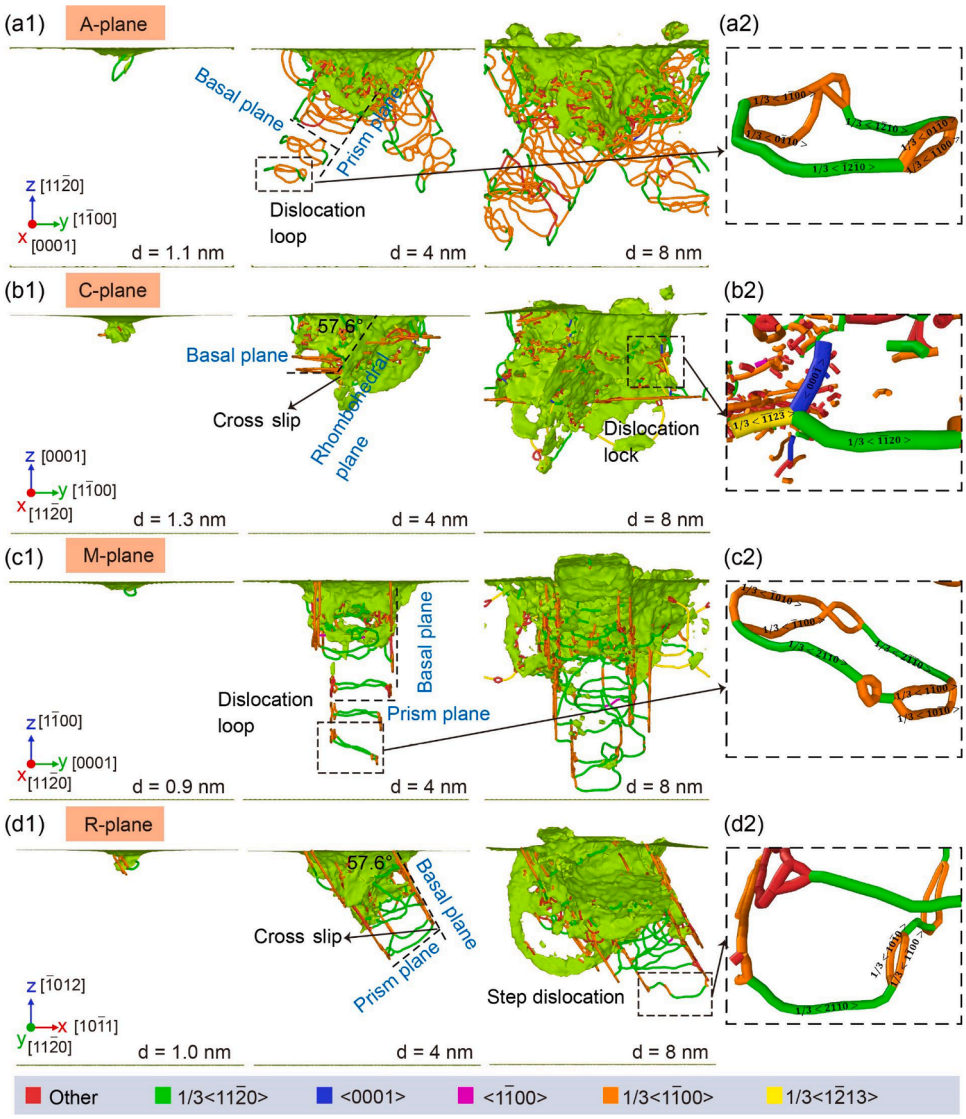

Fig. 6. Subsurface DXA analysis of sapphire after nanoindentation on different crystallographic planes: (a1-d1) Dislocation characteristics at various depths, including the critical depth for the elastic-plastic transition and at depths of 4 nm and 8 nm (with green, blue, light red, orange, yellow, and red indicating different types of dislocations); (a2-d2) Magnified views of dislocation interactions corresponding to the subsurface deformation regions shown in (a1-d1).

indentations on the other crystallographic planes, as detailed in **Appendix A5**. The TEM images in the experiment verify the slip systems that appear in the MD simulations. Specifically, nanoindentation of A/M-plane primarily activates BS and prismatic slip (PS). The C-plane mainly activates BS and RS, with BS being activated first. For the R-plane, BS, PS, and RS are activated during the nanoindentation process.

3.3.2. Twinning and fracture

In single-crystal materials, twinning often serves as the "last line" of plastic defense. Through analyzing twinning formation, the origins of crack initiation can be identified, providing insight into strategies for reducing subsurface damage.

The variation in the number of twinning atoms generated in the A/C/M/R-planes at different indentation depths is illustrated in Fig. 9 **(a1-d1)**. Basal twinning (BT) first appears in the subsurface of the A-plane at an indentation depth of 2 nm. The number of atoms in BT shows an overall upward trend as the indentation depth increases. Rhombohedral twinning (RT) appears at a depth of 4 nm, where the number of RT atoms initially increases and then stabilizes. However, prismatic twinning (PT) only appears at a depth of 8 nm. For the C-plane, the first appearance of BT occurs at a depth of 1.5 nm. As the indentation depth increases, the number of BT atoms first increases and then decreases, showing periodic fluctuations, similar to the results in the literature [52]. These fluctuations are attributed to the interaction between RS and BT due to increased stress. RT appears at a depth of 2.5 nm, with its atom count initially rising, then decreasing, and finally stabilizing. The number of PT atoms remains nearly constant and close to zero throughout the process. BT appears in the M-plane when the depth exceeds 2 nm. Initially, the number of BT atoms increases slightly, followed by a steep growth trend. The number of BT atoms decreases as the basal slip moves toward the bottom of the substrate. The appearance of PT lags slightly behind BT, with a critical indentation depth of 3 nm, after which the number of PT atoms steadily increases. Only a few RT atoms are generated throughout the process. Compared to the A/C/M-planes, RT appears earlier on the R-plane and increases with indentation depth. It remains stable at an indentation depth of 6 nm. Then PT forms in the contact area, fluctuating within a stable range during the entire indentation process. BT nucleates last and eventually surpasses the number of the other two twinning types. The explosive growth of BT atoms at the final stage is driven by dense BS activity. While cracks caused by twinning are not directly observed in the MD simulations, they are instead manifested by atoms in an amorphous state.

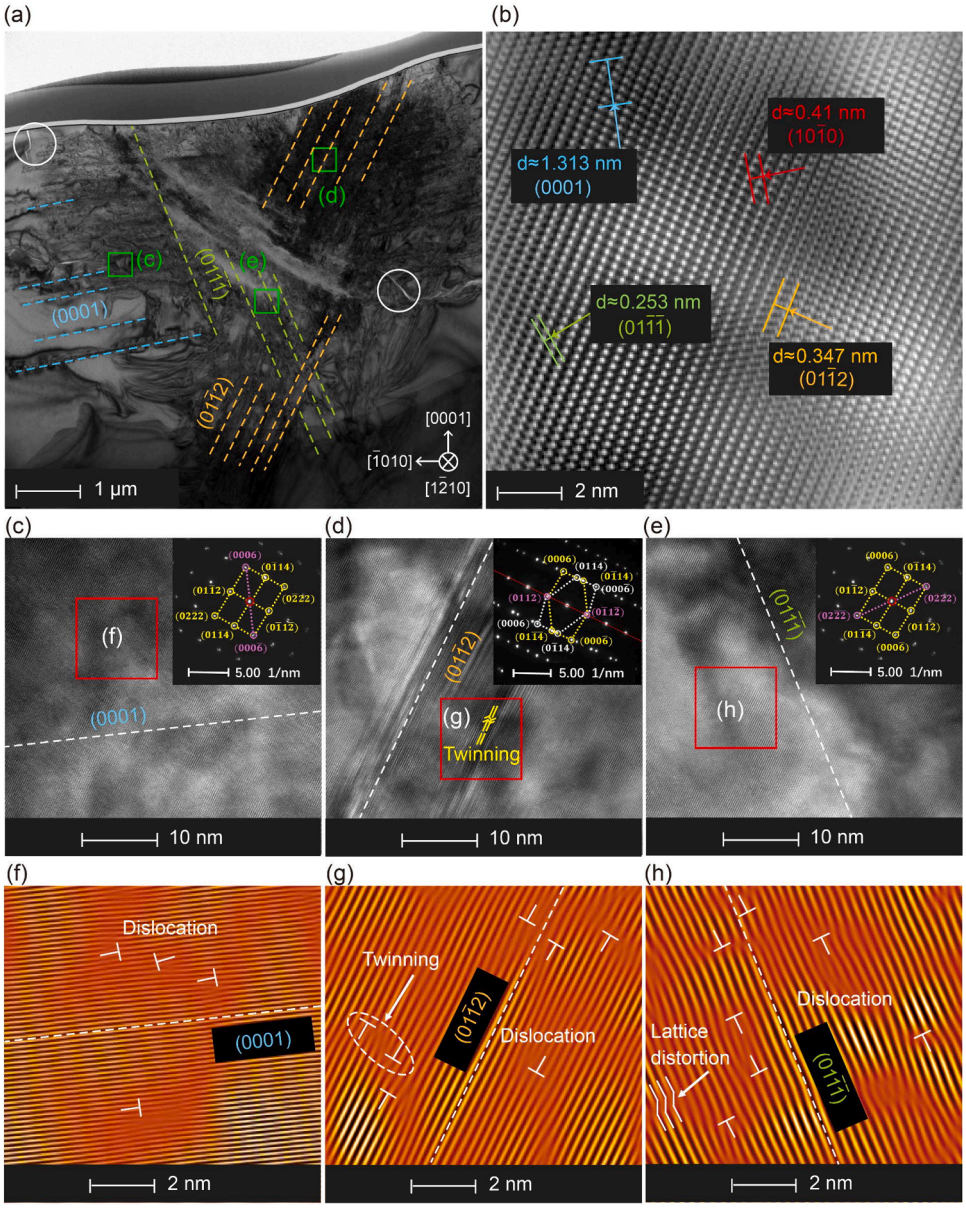

Fig. 7. TEM images of the subsurface region beneath nanoindentation on the C-plane: (a) Overall subsurface damage morphology beneath the indentation along the [1$\bar{2}$10] crystallographic direction; (b) Interplanar spacings of various crystallographic planes; (c–e) HR-TEM and SAED images of the subsurface damage region, revealing high-density stacking fault bands and twins; (f–h) FFT analyses corresponding to the regions highlighted in (c–e).

The formation of subsurface cracks of the A/C/M/R-planes under nanoindentation is shown in Fig. 9 **(a2-d2)**. For the A-plane, small cracks form along the (0001) and {11$\bar{2}$3} planes in the cross-section along the [1$\bar{1}$00] direction. These two cracks are located near the surface and propagate into the matrix in an interlaced manner. In contrast, only cracks along the (10$\bar{1}$2) plane is observed in the [0001] direction. The size of the crack is significantly larger than the previous two, and it is located farther from the surface. The cracks observed along different sections in the experiment are consistent with the twinning generated in the (0001), (11$\bar{2}$3), and (10$\bar{1}$2) planes by the MD simulations. However, the simulation also obtained twinning along the (11$\bar{2}$0) plane, which was not detected in the experimental results. This discrepancy could be attributed to the (11$\bar{2}$0) plane being parallel to the pressure surface, requiring higher energy for twinning formation compared to other crystal planes. Fig. 9**(b2)** illustrates the generation of cracks in the subsurface of the C-plane caused by twinning. A crack along the (11$\bar{2}$0) plane is observed in the cross-section along the [1$\bar{1}$00] direction, extending from the contact surface into the substrate. In another cross-section view, a small crack is found along the (10$\bar{1}$2) plane, located in the middle of the substrate. The experimental results are clearly consistent with the simulation results. However, the BT observed in the simulation was not seen in the experiment. The literature [89] has shown that the critical shear stress of BT is greater than that of RT, explaining this phenomenon. For the M-plane, the crack generated along the (11$\bar{2}$0) plane is significantly larger than those along the basal and rhombohedral planes, as shown in Fig. 9**(c2)**. Furthermore, BT formation is also observed on the (11$\bar{2}$0) section. In the R-plane, large cracks are seen on the contact surface of the indentation, aligned parallel to the (11$\bar{2}$0) plane. In the cross-section along the [11$\bar{2}$0] direction, small cracks form along the (0001) plane, as shown in Fig. 9**(d2)**. Although the MD simulations results show that the number of PT atoms is minimal, their propagation direction is parallel to the loading force. The difference in the direction of the loading force accounts for the difference in crack size. Additionally, no cracks caused by RT were observed in the

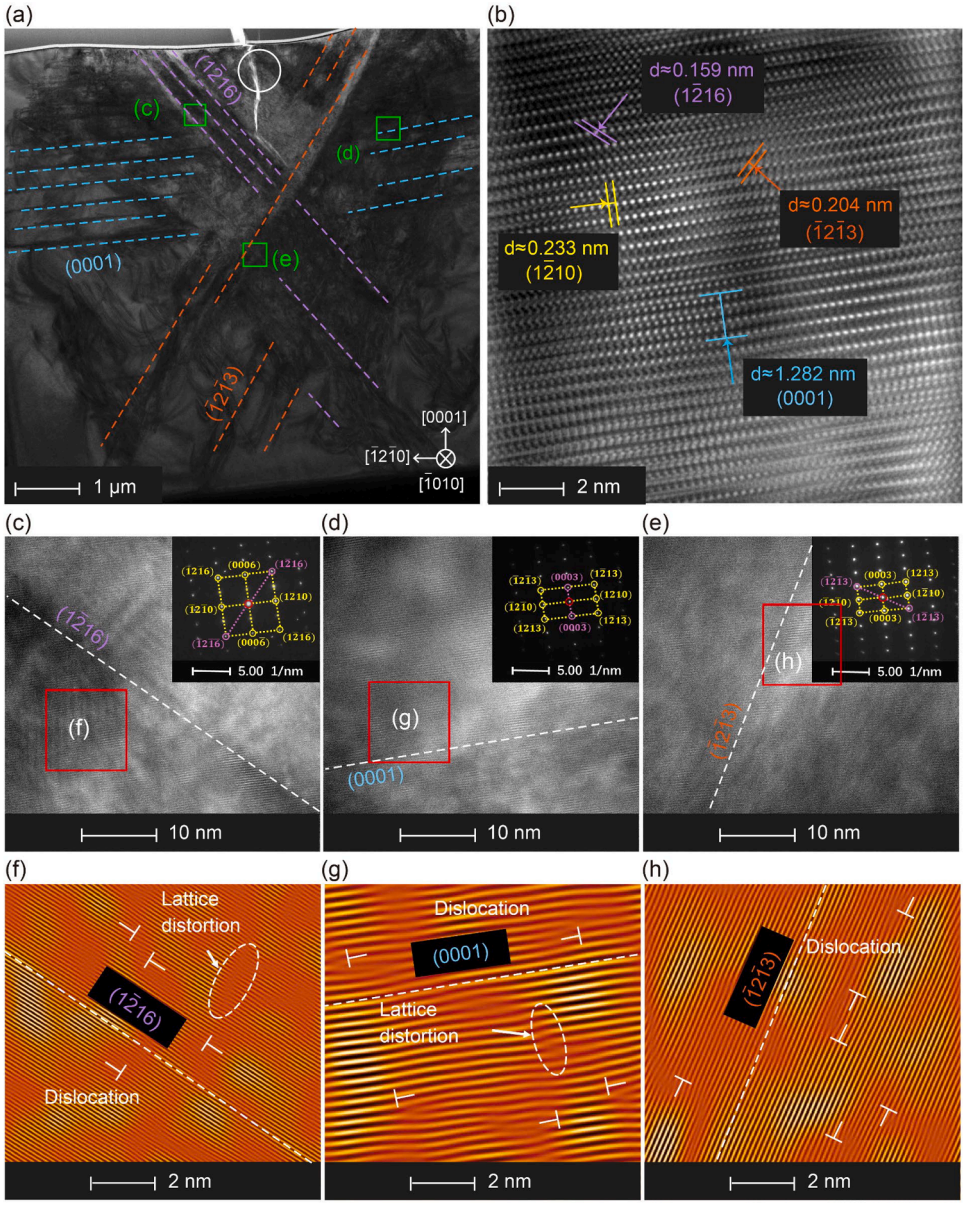

Fig. 8. TEM images of the subsurface region beneath nanoindentation on the C-plane: (a) Overall subsurface damage morphology beneath the indentation along the [$\bar{1}$010] crystallographic direction; (b) Interplanar spacings of various crystallographic planes; (c–e) HR-TEM and SAED images of the subsurface damage region, revealing high-density stacking fault bands and lattice distortion; (f–h) FFT analyses corresponding to the regions highlighted in (c–e).

experiment, similar to the absence of PT observed on the A-plane.

Therefore, under nanoindentation, the SSD of A/C-plane primarily produces cracks formed by BT and RT. The subsurface cracks of the M-plane primarily form by BT and PT, with BT formation facilitating the subsequent formation of PT, which serves as the main source of SSD cracks. The cracks generated by SSD on the R-plane are mainly caused by BT and PT.

4. Theoretical model of SSD evolution

As previously discussed, understanding slip deformation and twinning fracture is essential for controlling subsurface damage. However, the competitive behavior among different slip systems under varying indentation conditions is difficult to observe experimentally. Therefore, this section introduces a mechanical model that links indentation force to plastic deformation, explicitly accounting for contact stress and its directional dependence. The aim is to understand and predict the dynamic evolution of subsurface damage (SSD) in sapphire under nanoindentation conditions and provide a reference for future research and development of new analytical models and provide a reference for future research and development of new analytical models.

4.1. Loading force

During nano-indentation, the stress caused by the normal load does not fully reflect the actual slip deformation of the crystal. This paper infers stress from the contact area between the indenter and the substrate, as illustrated in Fig. 10**(a)**.

The plastic deformation force F_c [90], which is generated by the slip deformation of the material under external load, expresses as:

$$dF_c = F_p r^2 \sin\theta d\theta d\alpha, \tag{1}$$

where F_p is the unit plastic deformation force, r is the radius of the indenter, θ is the angle between the chip deformation force and centerline of the indenter, α is the angle between the direction of F_c and

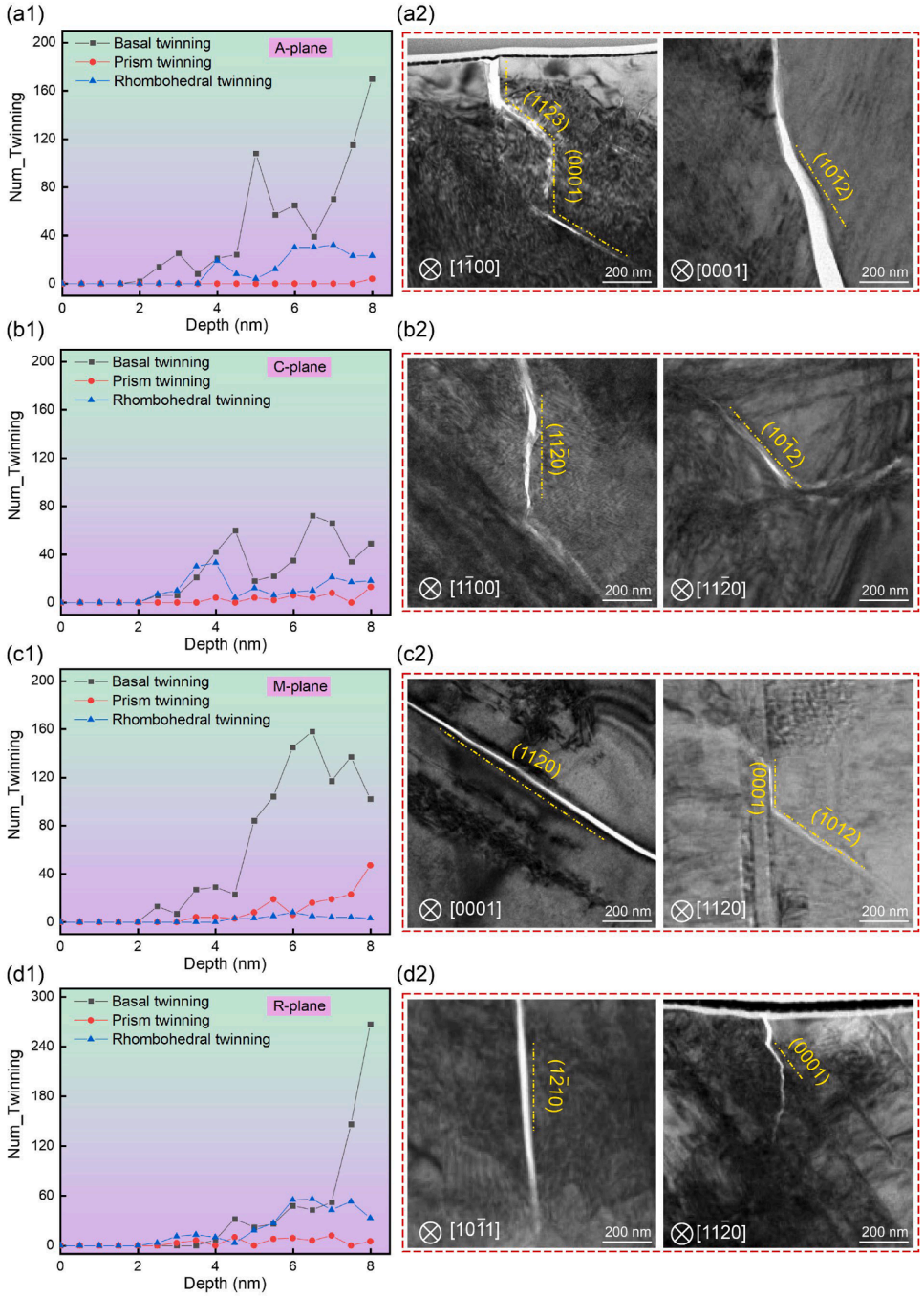

Fig. 9. Subsurface twinning analysis after nanoindentation on the A/C/M/R-planes. (a1-d1) Variation in the number of twinned atoms with indentation depth for different crystal planes; (a2-d2) Corresponding crystal cracks induced by twinning on different crystal planes.

the x-axis.

In this case, the chip deformation force can be divided into the tangential force, dF_x, along the x-axis, and normal force, dF_z, along the z-axis, as expressed as

$$\begin{cases} dF_x = F_p r^2 (\sin\theta)^2 d\theta d\alpha \\ dF_z = F_p r^2 sin\theta cos\theta d\theta d\alpha \end{cases}, \tag{2}$$

As only half a sphere ($\alpha=\pi/2$) is considered in the nanoindentation process, one can obtain the following relationship:

$$\begin{cases} F_x = \dfrac{\pi}{2} F_p r^2 (sin2\theta - 2\theta) \\ F_z = \dfrac{\pi}{4} F_p r^2 cos2\theta \end{cases}. \tag{3}$$

4.2. Schmid's factor

Schmid's law describes the plastic deformation tendency of the material by determining how easily the crystal slip system is activated. The relationship is as follows [91]:

$$u_i = \cos\lambda \cos\varphi, \tag{4}$$

where u_i is the Schmid's factor of the ith slip system, λ is the angle between the direction of F_c and the normal to the slip/twinning plane, and φ is the angle between the direction of F_c and slip direction of slip/twinning plane, as shown in Fig. 10**(b)**.

The plastic deformation parameter P_i (where a higher the P value

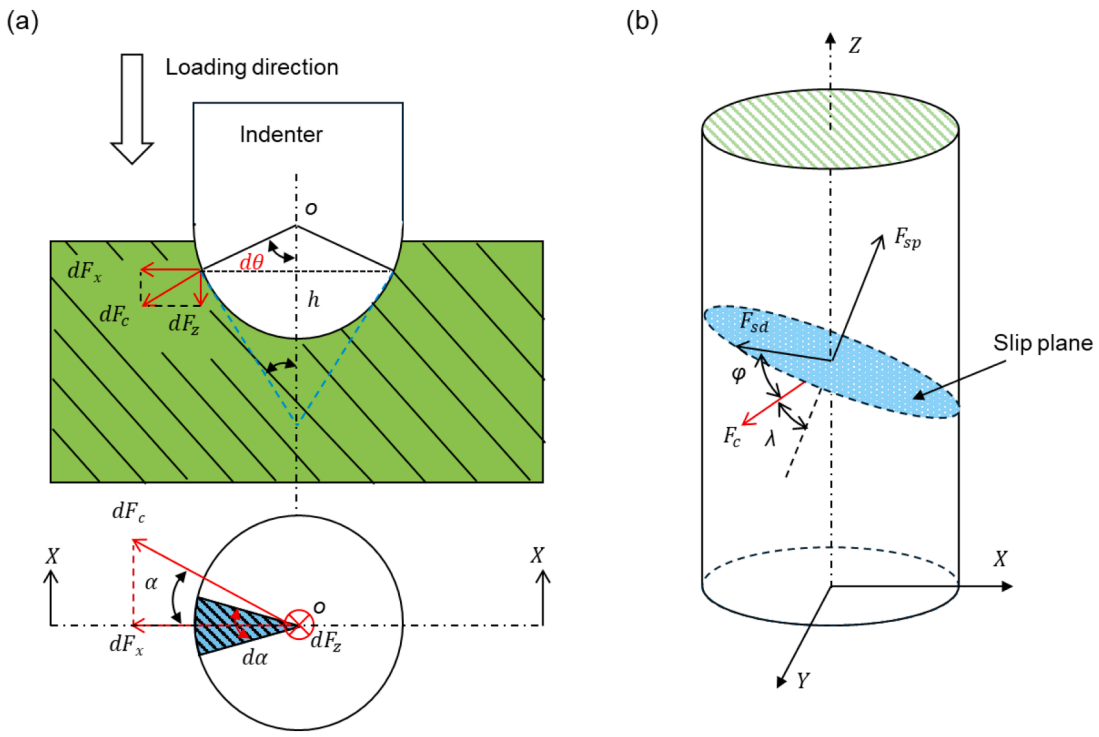

Fig. 10. Schematic diagram of the indenter-workpiece interaction during the nanoindentation process. (a) Cross-sectional view of the geometric-mechanical model of the indentation contact region (b) Spatial geometric relationship between the contact force (F_c) and slip plane. The F_c is decomposed into two components: F_{sp}, normal to the slip plane, and F_{sd}, parallel to the slip direction.

indicates a greater tendency for slip deformation in the slip systems) describes the activation degree of the slip deformation. The expression of P_i is as follows,

$$P_i = u_i d_{hkl}. \tag{5}$$

By computing the generalized stacking fault energy (GSFE) for multiple crystal planes and slip directions, we observed a clear correlation between interplanar spacing and the ease of slip activation [36]. Temperature also affects sapphire's plastic deformation: GSFE decreases on all planes as temperature rises. Analysis of both indentation experiments and molecular dynamics simulations shows that, although absolute GSFE values change with temperature, the relative trend in slip-activation difficulty among different planes remains unchanged (**Appendix A4**). To simplify our model, we have omitted temperature dependence from the present formulation.

4.3. Validation of theoretical model

This section presents a comprehensive validation of the previously proposed slip system activation model. By directly comparing theoretical predictions with results from MD simulations, the analysis focuses on how different slip systems are activated during nanoindentation across various crystallographic orientations of sapphire. Furthermore, the critical relationship between slip system activation and subsurface damage depth is emphasized, reinforcing theoretical predictions with evidence from MD simulations.

The calculated plastic deformation parameters for different sapphire crystal planes are shown on Fig. 11, where only common slip systems are considered. The order of activated slip systems varies significantly with changes in indentation depth. Although many slip systems are activated initially, the material only undergoes elastic deformation at this stage, as shown on the left side of the black dashed line in Fig. 12. After plastic deformation, indentation along the A-plane first activates the $(11\bar{2}3)\langle 01\bar{1}0\rangle$ slip system, followed by $(1\bar{2}10)\langle 10\bar{1}0\rangle$ and $(0001)\langle 11\bar{2}0\rangle$, and finally $(11\bar{2}3)\langle 11\bar{2}0\rangle$. Increasing indentation depth causes the $(0001)\langle 11\bar{2}0\rangle$ slip system to dominate during nanoindentation process of the A-plane. During nanoindentation of the C-plane, the $(0001)\langle 11\bar{2}0\rangle$ slip system is first triggered, followed by the activation of $(\bar{2}110)\langle 01\bar{1}0\rangle$, and finally the activation of $(11\bar{2}3)\langle 11\bar{2}0\rangle$ and $(01\bar{1}2)\langle\bar{2}021\rangle$. As the indentation depth increases, the activation of the $(0001)\langle 11\bar{2}0\rangle$ slip system gradually decreases, while the activation of $(11\bar{2}3)\langle 11\bar{2}0\rangle$ and $(01\bar{1}2)\langle\bar{2}021\rangle$ gradually increases. Indentation along the M-plane first activates the $(\bar{2}110)\langle 01\bar{1}0\rangle$ slip system, followed by $(0001)\langle 11\bar{2}0\rangle$, and finally $(11\bar{2}3)\langle 11\bar{2}0\rangle$ and $(01\bar{1}2)\langle\bar{2}021\rangle$. The increase in indentation depth results in the activation of $(0001)\langle 11\bar{2}0\rangle$ being much higher than that of other slip systems, similar to the behavior in the A-plane. Indentation along the R-plane first activates the $(0001)\langle 11\bar{2}0\rangle$ slip system, followed by $(01\bar{1}2)\langle 1\bar{1}01\rangle$ and $(10\bar{1}0)\langle 11\bar{2}0\rangle$, and finally $(01\bar{1}4)\langle 1\bar{1}01\rangle$. As the indentation depth increases, the activation of $(0001)\langle 11\bar{2}0\rangle$ and $(01\bar{1}2)\langle 1\bar{1}01\rangle$ become higher, but the $(0001)\langle 11\bar{2}0\rangle$ slip system remains dominant. In crystal slip analysis, slip systems with lower plastic deformation parameters can be ignored [92]. Therefore, during the subsequent stages of indentation, the main plastic deformation is BS in the A/M-plane, RS in the C-plane, and a combination of BS and RS in the R-plane. The above theoretical calculation results effectively explain the MD simulations observations, as shown in Fig. 5.

The type of activated slip system determines the SSD depth of the indentation. The changes in the SSD depth of the A/C/M/R-plane as the indentation depth increases are shown in Fig. 12**(a)**. The SSD depth of the A-plane initially increases rapidly, then slows down, and finally increases rapidly again. It is consistent with the trend of the $(0001)\langle 11\bar{2}0\rangle$ slip system observed in theoretical calculations. The SSD depth of the M-plane first increases, then stabilizes, and finally increases again. Although the trend of the $(0001)\langle 11\bar{2}0\rangle$ slip system is consistent in the theoretical calculations for both the A-plane and M-plane, there is a significant difference in the SSD depth changes. Due to the larger indentation depth, the M-plane activates more slip systems compared to

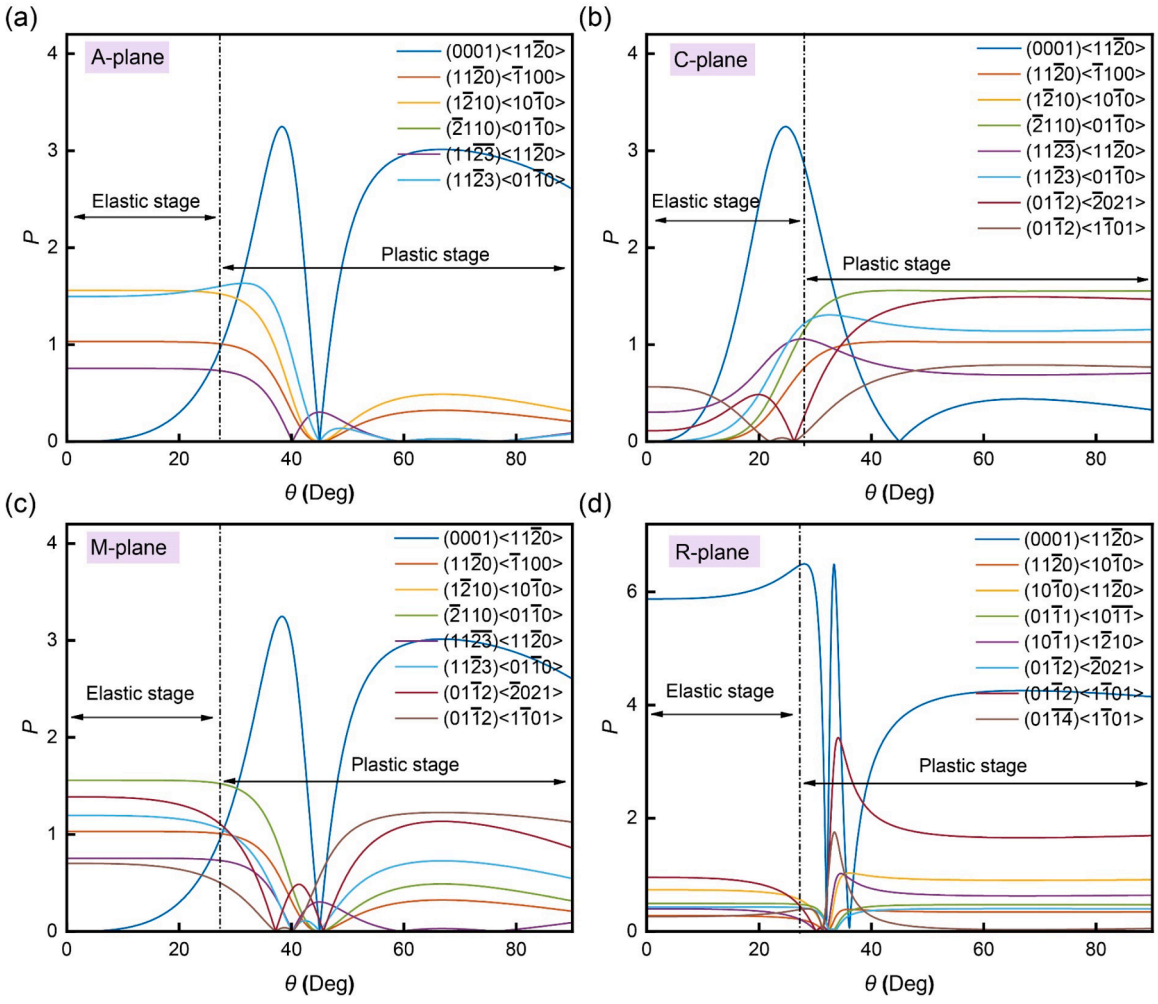

Fig. 11. Variation of subsurface slip system activation with angle under nanoindentation for different crystallographic planes. The black dashed line denotes the critical threshold for elastic–plastic deformation. The angle magnitude corresponds to the indentation depth. P represents the ease of slip system activation—the larger the value, the easier the slip. Colored curves represent different slip systems. (a) A-plane; (b) C-plane; (c) M-plane; (d) R-plane.

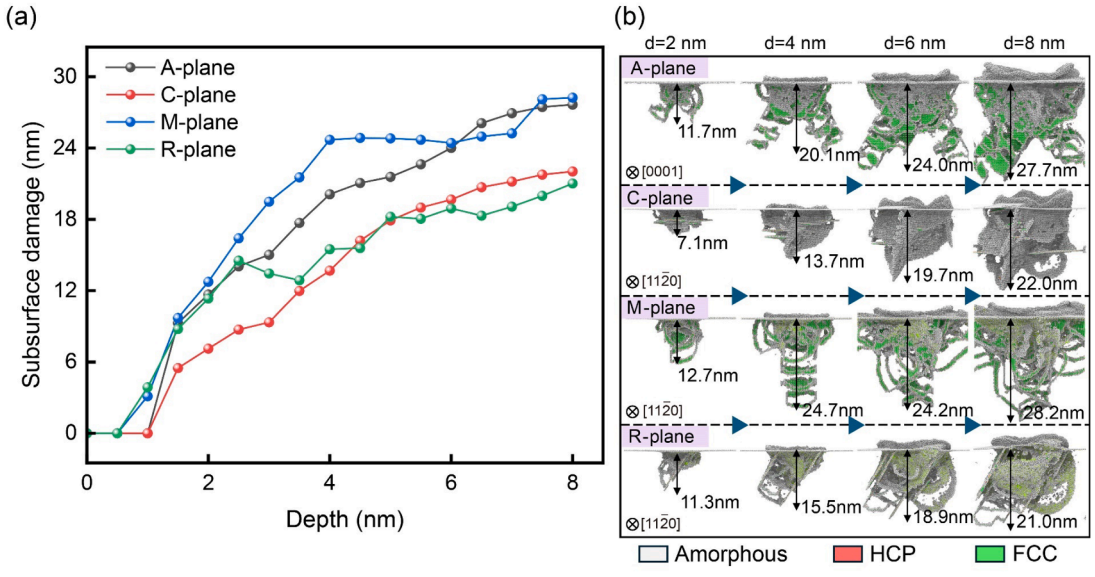

Fig. 12. Subsurface damage depth during MD simulations of nanoindentation. (a) Variation of SSD with increasing indentation depth for different crystallographic planes; (b) Evolution of SSD at different depths: $d = 2, 4, 6, 8$ nm.

the A-plane. The increased number of active slip systems leads to greater interaction activity, which delays the movement of the main slip system. However, the SSD depth of the M-plane is significantly greater than that of the A-plane. It occurs because the activated basal slip system in the M-plane forms a 90° angle with the compression surface, compared to a 60° angle in the A-plane, as shown in Fig. 12**(b)**. The R-plane exhibits a trend like that of the A-plane, as the activated $(0001)\langle 11\bar{2}0\rangle$ slip system forms 57.6° angle with the compressed surface. Although the activation of complex slip systems ultimately reduces the SSD depth, an overall growth trend is still observed. The SSD depth of the C-plane increases with indentation depth. When the indentation depth is less than 4 nm, the C-plane exhibits the minimal damage depth. In addition, its damaged depth remains relatively controlled. When the indentation depth is less than 2 nm, the SSD is primarily manifested as BS. As the indentation depth increases, RS becomes more dominant, contributing to the SSD depth increase. This feature is also reflected in theoretical calculations.

5. Conclusions

This study provides a comprehensive insight into the anisotropic of plastic deformation and subsurface damage evolution in sapphire during nanoindentation. Based on a detailed combination of MD simulations, experimental nanoindentation tests, SEM and TEM characterization, and theoretical modeling, the investigation systematically explains how crystallographic orientation affects the initiation and development of deformation and damage in sapphire.

The experimental and simulation results reveal the significant anisotropy in slip system activity and crack propagation across different crystallographic planes. The basal plane serves as the preferred slip plane for the A/M/R-planes, while the R-plane is the preferred slip plane for the C-plane. Cracks preferentially nucleate and propagate along the twinning planes, with basal and rhombohedral twinning playing key roles. Furthermore, the activation and interaction of slip systems and twinning mechanisms significantly influence the depth and distribution of subsurface damage. For the A/M/R-plane, BS primarily governs SSD depth, following the depth trend M-plane > A-plane > R-plane. For the C-plane, BS initially dominates, resulting in minimal damage at shallow indentations; however, as indentation depth increases, RS becomes dominant, increasing the damage depth substantially.

To rationalize these behaviors, a theoretical model was proposed to predict the activation priority of different slip systems based on crystallography and loading conditions. This model accurately reproduces the competitive behavior of slip systems across orientations and depths, providing an essential theoretical foundation for optimizing sapphire machining processes. And it can be extended to predict and control damage in other anisotropic crystalline materials.

Overall, the present work advances the mechanistic understanding of plastic deformation and damage evolution in sapphire and provides valuable insights for the development of optimized, low-damage ultra-precision machining strategies.

CRediT authorship contribution statement

Yuqiang Zhang: Writing – original draft, Data curation. **Zhongwei Hu:** Supervision, Funding acquisition, Conceptualization. **Yiqing Yu:** Writing – review & editing, Funding acquisition. **Xipeng Xu:** Writing – review & editing, Methodology. **Xintian Cai:** Writing – review & editing. **Qing Peng:** Writing – review & editing, Supervision, Funding acquisition. **Wenhan Zeng:** Writing – review & editing. **Wenbin Zhong:** Writing – review & editing. **Liam Blunt:** Writing – review & editing, Formal analysis. **Xiangqian Jiang:** Supervision, Project administration, Funding acquisition.

Declaration of competing interest

The authors declare that they have no known competing financial interests or personal relationships that could have appeared to influence the work reported in this paper.

Acknowledgments

This research was funded by the National Natural Science Foundation of China (Grant No. 52175404, 52375429, 12272378), and The Future Advanced Metrology Hub for Sustainable Manufacturing (Ref: EP/Z53285X/1).

Supplementary materials

Supplementary material associated with this article can be found, in the online version, at doi:10.1016/j.ijmecsci.2025.110769.

Data availability

Data will be made available on request.

References

[1] Wang S, Wang S, Zhao Q. Residual stress and subsurface damage in sapphire ultra-precision grinding. J Mater Process Technol 2024;328:118418. https://doi.org/10.1016/j.jmatprotec.2024.118418.
[2] Maas P, Mizumoto Y, Kakinuma Y, et al. Anisotropic brittle-ductile transition of monocrystalline sapphire during orthogonal cutting and nanoindentation experiments. Nanotechnol Precis Eng 2018;1(3):157–71. https://doi.org/10.1016/j.npe.2018.09.005.
[3] Kwon SB, Nagaraj A, Xi D, et al. Studying crack generation mechanism in single-crystal sapphire during ultra-precision machining by MD simulation-based slip/fracture activation model. Int J Precis Eng Manuf 2023;24(5):715–27. https://doi.org/10.1016/j. precisioneng.2023.12.007.
[4] Huang S, Li X, Zhao Y, et al. A novel lapping process for single-crystal sapphire using hybrid nanoparticle suspensions. Int J Mech Sci 2021;191:106099. https://doi.org/10.1016/j.ijmecsci.2020.106099.
[5] Li H, Wu H, Zhang Q, et al. Study of β-Ga_2O_3 (001) /sapphire (a-plane) heterostructure in wide bandgap solar-blind deep-ultraviolet photodetector. J Cryst Growth 2024;628:127513. https://doi.org/10.1016/j.jcrysgro.2023.127513.
[6] Chen HG, Le PH, Teng IJ, et al. Microstructures and mechanical properties of Sb-doped ZnO thin films deposited on a-plane sapphire substrates. Ceram Int 2024;50(1):614–21. https://doi.org/10.1016/j.ceramint.2023.10.139.
[7] Butanovs E, Zubkins M, Strods E, et al. Impact of temperature and film thickness on α-and β-phase formation in Ga_2O_3 thin films grown on A-plane sapphire substrate. Thin Solid Films 2024;803:140467. https://doi.org/10.1016/j.tsf.2024.140467.
[8] Zou Y, Niu X, Zhan N, et al. Effect of amino acid complexing agents on chemical mechanical polishing performance and action mechanism of C-plane sapphire: combining experiments and theoretical calculations. Mater Chem Phys 2024;316:129066. https://doi.org/10.1016/j.matchemphys.2024.129066.
[9] Jung IY, Song S, Choi M, et al. Evolution of mechanically formed bow due to surface waviness and residual stress difference on sapphire (0001) substrate. J Mater Process Technol 2019;269:102–8. https://doi.org/10.1016/j.jmatprotec.2019.02.003.
[10] Liu D, Qi Y, Chen J, et al. Effect of temperature on the mechanical properties and anisotropy of C-plane sapphire: insights from indentation tests and MD simulations. Vacuum 2025;237:114187. https://doi.org/10.1016/j.vacuum.2025.114187.
[11] Takane H, Konishi S, Hayasaka Y, et al. Structural characterization of threading dislocation in α-Ga_2O_3 thin films on c-and m-plane sapphire substrates. J Appl Phys 2024;136(2). https://doi.org/10.1063/5.0206863.
[12] Li Z, Zhang X, Zhang L, et al. Improving the quality of MOCVD-grown α-Ga_2O_3 by introducing an AGO buffer on m-plane sapphire. Vacuum 2025:114445. https://doi.org/10.1016/j.vacuum.2025.114445.
[13] Li Z, Zhang X, Zhang L, et al. Suppression of screw dislocation-induced hillocks in MOCVD-grown α-Ga_2O_3 on m-plane sapphire by introducing a high-temperature buffer. Cryst Growth Des 2025. https://doi.org/10.1021/acs.cgd.4c01472.
[14] Naritsuka S, Kato Y, Nonogaki M, et al. A-plane GaN microchannel epitaxy on R-plane sapphire substrate using patterned graphene mask. J Cryst Growth 2024;630:127593. https://doi.org/10.1016/j.jcrysgro.2024.127593.
[15] Zhang YN, Lin B, Li ZC. An overview of recent advances in Chemical Mechanical Polishing (CMP) of sapphire substrates. ECS Trans 2013;52(1):495. https://doi.org/10.1149/05201.0495ecst.
[16] Wang W, Yang W, Wang H, et al. A comparative study on the properties of C-plane and A-plane GaN epitaxial films grown on sapphire substrates by pulsed laser deposition. Vacuum 2016;128:158–65. https://doi.org/10.1016/j.vacuum.2016.03.032.

[17] Singh AP, Vajire SL, Mishra D. Nanoindentation simulation of gallium nitride grown in different orientations on a sapphire substrate using finite element method. Mater Today: Proc 2023;79:282–5. https://doi.org/10.1016/j.matpr.2022.11.201.
[18] Liu J, Deng H, Zhao X, et al. Investigation of the nano and micromechanical performance of β-Ga_2O_3 epitaxial films on sapphire using nanoindentation. Vacuum 2024:113413. https://doi.org/10.1016/j.vacuum.2024.113413. -TEM.
[19] Mahmoud ZH, AL-Salman HNK, Kianfar E. Nanoindentation: introduction and applications of a non-destructive analysis. Nano Trans Med 2024:100057. https://doi.org/10.1016/j.ntm.2024.100057.
[20] Pshyk O, Nakonechna O, Coy E. Current view of nanoindentation: recent developments and application in material characterization. ACS Appl Mater Interfaces 2025. https://doi.org/10.1021/acsami.5c05434.
[21] Long X, Li Y, Shen Z, et al. Review of uniqueness challenge in inverse analysis of nanoindentation. J Manuf Process 2024;131:1897–916. https://doi.org/10.1016/j.jmapro.2024.10.005.
[22] Li L, Du JP, Ogata S, et al. Variation of first pop-in loads in nanoindentation to detect chemical short-range ordering in the equiatomic Cr-Co-Ni medium-entropy alloy. Acta Mater 2024;269:119775. https://doi.org/10.1016/j.actamat.2024.119775.
[23] Shen Z, Dong R, Li J, et al. Determination of gradient residual stress for elastoplastic materials by nanoindentation. J Manuf Process 2024;109:359–66. https://doi.org/10.1016/j.jmapro.2023.10.030.
[24] Babuska TF, Mings A, Larson SR, et al. Microstructural assessment of molybdenum disulfide coatings using nanoindentation hardness. ACS Appl Mater Interfaces 2025. https://doi.org/10.1021/acsami.4c18369.
[25] Texier D, Richeton T, Proudhon H, et al. Increase in elastic and hardness anisotropy of titanium with oxygen uptake due to high temperature oxidation: a multimodal framework using high speed nanoindentation mapping. Mater Charact 2024;216:114244. https://doi.org/10.1016/j.matchar.2024.114244.
[26] Zhu F, Zhang Q, Chen J, et al. Effect of crystallographic orientation on the deformation and mechanical behavior of CoCrFeNi in Berkovich nanoindentation. Mater Sci Eng: A 2024;914:147106. https://doi.org/10.1016/j.msea.2024.147106.
[27] Fan P, Katiyar NK, Arshad M, et al. Anisotropic plasticity mechanisms in a newly synthesised high entropy alloy investigated using atomic simulations and nanoindentation experiments. J Alloys Compd 2024;970:172541. https://doi.org/10.1016/j.jallcom.2023.172541.
[28] Zhang H, Huang H, Wang C, et al. Nanoindentation behaviors of the AlCoCrFeNi2.1 eutectic high-entropy alloy: the effects of crystal structures. J Alloys Compd 2024;1008:176535. https://doi.org/10.1016/j.jallcom.2024.176535.
[29] Guo Y, Staedler T, Müller J, et al. A detailed analysis of the determination of fracture toughness by nanoindentation induced radial cracks. J Eur Ceram Soc 2020;40(2):276–89. https://doi.org/10.1016/j.jeurceramsoc.2019.10.013-liewen.
[30] Li C, Zhang Q, Zhang Y, et al. Nanoindentation and nanoscratch tests of YAG single crystals: an investigation into mechanical properties, surface formation characteristic, and theoretical model of edge-breaking size. Ceram Int 2020;46(3):3382–93. https://doi.org/10.1016/j.ceramint.2019.10.048.
[31] Yan J, Takahashi H, Gai X, et al. Load effects on the phase transformation of single-crystal silicon during nanoindentation tests. Mater Sci Eng: A 2006;423(1–2):19–23. https://doi.org/10.1016/j.msea.2005.09.120.
[32] Matsumoto M, Huang H, Harada H, et al. On the phase transformation of single-crystal 4H–SiC during nanoindentation. J Phys D Appl Phys 2017;50(26):265303. https://doi.org/10.1088/1361-6463/aa7489.
[33] Lu C, Mai YW, Tam PL, et al. Nanoindentation-induced elastic–plastic transition and size effect in α-Al_2O_3 (0001). Philos Mag Lett 2007;87(6):409–15. https://doi.org/10.1080/09500830701203156.
[34] Mao WG, Shen YG, Lu C. Nanoscale elastic–plastic deformation and stress distributions of the C plane of sapphire single crystal during nanoindentation. J Eur Ceram Soc 2011;31(10):1865–71. https://doi.org/10.1016/j.jeurceramsoc.2011.04.012.
[35] Mao W, Shen Y. Nanoindentation study of pop-in phenomenon characteristics and mechanical properties of sapphire (10-12) crystal. J Am Ceram Soc 2012;95(11):3605–12. https://doi.org/10.1111/j.1551-2916.2012.05405.x.
[36] Yan S, Nawaz A, Islam B, et al. Elastic-plastic deformation behavior of sapphire M-plane under static loading using nano-indentation. Ceram Int 2021;47(16):23528–38. https://doi.org/10.1016/j.ceramint.2021.05.069.
[37] Wang N, Jiang F, Xu X, et al. Effects of crystal orientation on the crack propagation of sapphire by sequential indentation testing. Crystals 2017;8(1):3. https://doi.org/10.3390/cryst8010003.
[38] Ma Y, Cao L, Hang W, et al. Crystallographic orientation effect on the incipient plasticity and its stochastic behavior of a sapphire single crystal by spherical nanoindentation. Ceram Int 2020;46(10):15554–64. https://doi.org/10.1016/j.ceramint.2020.03.102.
[39] Trabadelo V, Pathak S, Saeidi F, et al. Nanoindentation deformation and cracking in sapphire. Ceram Int 2019;45(8):9835–45. https://doi.org/10.1016/j.ceramint.2019.02.022.
[40] Wang Y, Zhang S, Xia H, et al. Unveiling the effect of crystal orientation on gallium nitride cutting through MD simulation. Int J Mech Sci 2023;259:108619. https://doi.org/10.1016/j.ijmecsci.2023.108619.
[41] Liu J, Deng H, Zhao X, et al. Investigation of the nano and micromechanical performance of β-Ga_2O_3 epitaxial films on sapphire using nanoindentation. Vacuum 2024:113413. https://doi.org/10.1016/j.vacuum.2024.113413.
[42] Hu Z, Chen Y, Lai Z, et al. Coupling of double grains enforces the grinding process in vibration-assisted scratch: insights from molecular dynamics. J Mater Process Technol 2022;304:117551. https://doi.org/10.1016/j.jmatprotec.2022.117551.
[43] Chen Y, Hu Z, Jin J, et al. Molecular dynamics simulations of scratching characteristics in vibration-assisted nano-scratch of single-crystal silicon. Appl Surf Sci 2021;551:149451. https://doi.org/10.1016/j.apsusc.2021.149451.
[44] Meng B, Li C. Effect of anisotropy on deformation and crack formation under the brittle removal of 6H-SiC during SPDT process. J Adv Res 2024;56:103–12. https://doi.org/10.1016/j.jare.2023.04.004.
[45] Zhao J, Li W, Chen S, et al. Atomic-scale material removal and deformation mechanism in nanoscratching GaN. Int J Mech Sci 2025;285:109804. https://doi.org/10.1016/j.ijmecsci.2024.109804.
[46] Wang J, Yan Y, Cui H, et al. Towards understanding the mechanisms of material removal and deformation in Gaas during nanomilling. J Mater Process Technol 2025;337:118712. https://doi.org/10.1016/j.jmatprotec.2025.118712.
[47] Li T, Zhao P, Shang F. Wear behaviors and plastic deformation mechanisms induced by nano-grinding of indium-doped gallium nitride single crystal. Tribol Int 2024;197:109791. https://doi.org/10.1016/j.triboint.2024.109791.
[48] Nishimura K, Kalia RK, Nakano A, et al. Nanoindentation hardness anisotropy of alumina crystal: a molecular dynamics study. Appl Phys Lett 2008;92(16). https://doi.org/10.1063/1.2913016.
[49] Kim WK, Xi D, Kim BH. Nanoscale indentation and scratching tests of single crystal sapphire using molecular dynamics simulation. Comput Mater Sci 2019;170:109195. https://doi.org/10.1016/j.commatsci.2019.109195.
[50] Lin J, Jiang F, Xu X, et al. Molecular dynamics simulation of nanoindentation on c-plane sapphire. Mech Mater 2021;154:103716. https://doi.org/10.1016/j.mechmat.2020.103716.
[51] Xu Q, Zaborowska A, Mulewska K, et al. Atomistic insights into nanoindentation-induced deformation of α-Al2O3 single crystals. Vacuum 2024;219:112733. https://doi.org/10.1016/j.vacuum.2023.112733.
[52] Chen J, Qi Y, Liu D, et al. Alternate activation-annihilation of dislocations realizes the plasticity of sapphire during indentation. Mater Des 2024;239:112772. https://doi.org/10.1016/j.matdes.2024.112772.
[53] Qiu T, Jiang F, Wang N, et al. Atomistic understanding of the variable nano-hardness of C-plane sapphire considering the crystal anisotropy. J Mater Res Technol 2024;29:4514–25. https://doi.org/10.1016/j.jmrt.2024.02.161.
[54] Tochigi E, Miao B, Nakamura A, et al. Atomic-scale mechanism of rhombohedral twinning in sapphire. Acta Mater 2021;216:117137. https://doi.org/10.1016/j.actamat.2021.117137.
[55] Huang L, Bonifacio C, Song D, et al. Investigation into the microstructure evolution caused by nanoscratch-induced room temperature deformation in M-plane sapphire. Acta Mater 2011;59(13):5181–93. https://doi.org/10.1016/j.actamat.2011.04.054.
[56] Piao Y, Li C, Hu Y, et al. Nanoindentation induced anisotropy of deformation and damage behaviors of MgF_2 crystals. J Mater Res Technol 2024;28:4615–25. https://doi.org/10.1016/j.jmrt.2024.01.034.
[57] Li C, Piao Y, Zhang F, et al. Understand anisotropy dependence of damage evolution and material removal during nanoscratch of MgF2 single crystals. Int J Extreme Manuf 2022;5(1):015101. https://doi.org/10.1088/2631-7990/ac9eed.
[58] Wang Y, Liang Z, Zhao W, et al. Anisotropic cutting mechanisms on the surface quality in ultra-precision machining of R-plane sapphire. Appl Surf Sci 2023;622:156868. https://doi.org/10.1016/j.apsusc.2023.156868.
[59] Wang J, Yan Y, Li C, et al. Material removal mechanism and subsurface characteristics of silicon 3D nanomilling. Int J Mech Sci 2023;242:108020. https://doi.org/10.1016/j.ijmecsci.2022.108020.
[60] Wang H, Kang R, Bao Y, et al. Microstructure evolution mechanism of tungsten induced by ultrasonic elliptical vibration cutting at atomic/nano scale. Int J Mech Sci 2023;253:108397. https://doi.org/10.1016/j.ijmecsci.2023.108397.
[61] Liu T, Luo Z. Molecular dynamics study of the potential formation thickness of ultrafast laser induced sapphire crystal surface recast layer. Mater Sci Semicond Process 2024;176:108307. https://doi.org/10.1016/j.mssp.2024.108307.
[62] Niu K, Du X, Mi W, et al. Fabrication and characterization of heteroepitaxial Zn2GeO4 films on sapphire via radio frequency magnetron sputtering. Appl Phys Lett 2025;126(3). https://doi.org/10.1063/5.0244857.
[63] Liu Z, Ju W, Fang Y, et al. In-plane adaptive heteroepitaxy of 2D cesium bismuth halides with engineered bandgaps on c-sapphire. Adv Mater 2025;37(5):2413852. https://doi.org/10.1002/adma.202413852.
[64] Voyiadjis GZ, Yaghoobi M. Review of nanoindentation size effect: experiments and atomistic simulation. Crystals 2017;7(10):321. https://doi.org/10.3390/cryst7100321.
[65] Song E, Andani MT, Misra A. Investigation of grain size and geometrically necessary dislocation density dependence of flow stress in Mg-4Al by using nanoindentation. Acta Mater 2024;265:119633. https://doi.org/10.1016/j.actamat.2023.119633.
[66] Kwon SB, Nagaraj A, Xi D, et al. Studying crack generation mechanism in single-crystal sapphire during ultra-precision machining by MD simulation-based slip/fracture activation model. Int J Precis Eng Manuf 2023;24(5):715–27. https://doi.org/10.1007/s12541-023-00776-w.
[67] Wang W, Peng Q, Dai Y, et al. Distinctive nanofriction of graphene coated copper foil. Comput Mater Sci 2016;117:406–11. https://doi.org/10.1016/j.commatsci.2016.01.007.
[68] Wang H, Dong Z, Wang C, et al. Surface/subsurface formation mechanism of tungsten during ultrasonic elliptical vibration cutting. Int J Mech Sci 2024;262:108725. https://doi.org/10.1016/j.ijmecsci.2023.108725.
[69] Le CT, Nguyen TT, Nguyen TT, et al. Molecular dynamics simulation of phase transformation and mechanical behavior in Al_2O_3 model. Vacuum 2019;167:175–81. https://doi.org/10.1016/j.vacuum.2019.06.010.

[70] Houska J. Pathway for a low-temperature deposition of α-Al_2O_3: a molecular dynamics study. Surf Coat Technol 2013;235:333–41. https://doi.org/10.1016/j.surfcoat.2013.07.062.
[71] Bodur CT, Chang J, Argon AS. Molecular dynamics simulation of basal and pyramidal system edge dislocations in sapphire. J Eur Ceram Soc 2005;25(8):1431–9. https://doi.org/10.1016/j.jeurceramsoc.2005.01.022.
[72] Hernández NC, Sanz JF. Molecular dynamics simulations of Pd deposition on the α-Al_2O_3 (0001) surface. J Phys Chem B 2001;105(48):12111–7. https://doi.org/10.1021/jp0130517.
[73] Lin J, Jiang F, Wen Q, et al. Deformation anisotropy of nano-scratching on C-plane of sapphire: a molecular dynamics study and experiment. Appl Surf Sci 2021;546:149091. https://doi.org/10.1016/j.apsusc.2021.149091.
[74] Zhao Y, Peng X, Fu T, et al. Strengthening mechanisms of graphene coated copper under nanoindentation. Comput Mater Sci 2018;144:42–9. https://doi.org/10.1016/j.commatsci.2017.12.009.
[75] Stukowski A. Visualization and analysis of atomistic simulation data with OVITO–the Open Visualization Tool. Model Simul Mater Sci Eng 2009;18(1):015012. https://doi.org/10.1088/0965-0393/18/1/015012.
[76] Stukowski A, Bulatov VV, Arsenlis A. Automated identification and indexing of dislocations in crystal interfaces. Model Simul Mater Sci Eng 2012;20(8):085007. https://doi.org/10.1088/0965-0393/20/8/085007.
[77] Liu L, Li X, Zhang R, et al. Mechanical damage and failure mechanisms of chlorite by molecular dynamics. Results Eng 2025;25:103898. https://doi.org/10.1016/j.rineng.2024.103898.
[78] Zhu J, Liu X, Zhou X, et al. Strengthening effect of graphene-edge dislocation interaction in graphene reinforced copper matrix composites. Comput Mater Sci 2021;188:110179. https://doi.org/10.1016/j.commatsci.2020.110179.
[79] Wang H, Dong Z, Kang R, et al. Surface characteristics and material removal mechanisms during nanogrinding on C-face and Si-face of 4H-SiC crystals: experimental and molecular dynamics insights. Appl Surf Sci 2024;665:160293. https://doi.org/10.1016/j.apsusc.2024.160293.
[80] Li C, Zhang F, Wang X, et al. Repeated nanoscratch and double nanoscratch tests of Lu_2O_3 transparent ceramics: material removal and deformation mechanism, and theoretical model of penetration depth. J Eur Ceram Soc 2018;38(2):705–18. https://doi.org/10.1016/j.jeurceramsoc.2017.09.028.
[81] ElFallagh F, Lockwood A, Inkson B. In-situ TEM observation of deformations in a single crystal sapphire during nanoindentation. Exp Numer Investig Adv Mater Struct 2013:229–39. https://doi.org/10.1007/978-3-319-00506-5_16.
[82] Li L, Sun X, Guo Y, et al. Nanoindentation response of monocrystalline copper under various tensile pre-deformations via molecular dynamic simulations. Adv Mech Eng 2018;10(12). https://doi.org/10.1177/1687814018816874.
[83] Tymiak NI, Gerberich WW. Initial stages of contact-induced plasticity in sapphire. I. surface traces of slip and twinning. Philos Mag 2007;87(33):5143–68. https://doi.org/10.1080/14786430701618464.
[84] Tymiak N, Chrobak D, Gerberich W, et al. Role of competition between slip and twinning in nanoscale deformation of sapphire. Phys Rev B 14Condensed Matter Mater Phys 2009;79(17):174116. https://doi.org/10.1103/PhysRevB.79.174116.
[85] Rezaee-Hajidehi M, Sadowski P, Stupkiewicz S. Deformation twinning as a displacive transformation: finite-strain phase-field model of coupled twinning and crystal plasticity. J Mech Phys Solids 2022;163:104855. https://doi.org/10.1016/j.jmps.2022.104855.
[86] Tymiak NI, Gerberich WW. Initial stages of contact-induced plasticity in sapphire. II. mechanisms of plasticity initiation. Philos Mag 2007;87(33):5169–88. https://doi.org/10.1080/14786430701618472.
[87] Lagerlöf KPD, Heuer AH, Castaing J, et al. Slip and twinning in sapphire (α-Al_2O_3). J Am Ceram Soc 1994;77(2):385–97. https://doi.org/10.1111/j.1151-2916.1994.tb07006.x.
[88] Montagne A, Pathak S, Maeder X, et al. Plasticity and fracture of sapphire at room temperature: load-controlled microcompression of four different orientations. Ceram Int 2014;40(1):2083–90. https://doi.org/10.1016/j.ceramint.2013.07.121.
[89] Huang L, Bonifacio C, Song D, et al. Investigation into the microstructure evolution caused by nanoscratch-induced room temperature deformation in M-plane sapphire. Acta Mater 2011;59(13):5181–93. https://doi.org/10.1016/j.actamat.2011.04.054.
[90] Zhang Y, Hu Z, Chen Y, et al. Insights into scratching force in axial ultrasonic vibration-assisted single grain scratching. J Manuf Process 2024;112:150–60. https://doi.org/10.1016/j.jmapro.2024.01.005.
[91] Mizumoto Y, Maas P, Kakinuma Y, et al. Investigation of the cutting mechanisms and the anisotropic ductility of monocrystalline sapphire. CIRP Ann 2017;66(1):89–92. https://doi.org/10.1016/j.cirp.2017.04.018.
[92] Hayama Y, Fujii S, Tanabe T, et al. Theoretical approach on the critical depth of cut of single crystal MgF2 and application to a microcavity. Precis Eng 2022;73:234–43. https://doi.org/10.1016/j.precisioneng.2021.09.002.